



Research Paper

Investigation on heat transfer characteristic of deformable high aspect-ratio biomass particle system in rotary drums with baffles



Conghui Gu^{a,*}, Yufan Zhang^a, Yuan Liu^a, Huiqian Yin^a, Xingyu Liang^a, Jingyu Zhu^a, Kaiyuan Deng^a, Zhulin Yuan^b

^a School of Energy and Power, Jiangsu University of Science and Technology, Zhenjiang, Jiangsu, 212100, China

^b Key Laboratory of Energy Thermal Conversion and Control of Ministry of Education, School of Energy and Environment, Southeast University, Nanjing, 210096, China

ARTICLE INFO

ABSTRACT

Keywords:

Particle-scale modelling
Baffle design
Thermal conduction
Computational fluid dynamics
Discrete element method

With the development of carbon reduction technologies, the energy conversion efficiency of the wet biomass particle system has attracted increasing attention. Heat transfer within these systems is a critical factor influencing combustion performance. In this study, experimental and simulation methods were used to investigate the behaviour of deformable high aspect-ratio biomass particles within different structural rotary drums. The particle heat transfer model of deformable high aspect-ratio biomass particles was established and validated. By comparing the simulation results with experimental data, good consistency was demonstrated. It systematically investigates the effects of drum rotation speed, the number of baffles, and drum temperature on the mixing and heat transfer processes of the biomass particle system. It was found that increasing the drum rotation speed facilitates heat transfer in the particles. The best heat transfer efficiency was observed at a speed of 10 r min⁻¹. As the mixing index improved, the heat exchange between particles became more efficient, and higher mixing index led to improved heat transfer efficiency. The highest mixing index reached 0.55, resulting in a notable increase in temperature. Moreover, increasing the number of baffles improved the uniformity of the particle temperature distribution, and optimising the drum temperature further enhanced heat transfer. The optimal results were achieved with 6 baffles and the drum wall temperature of 403.15 K. These findings provide valuable insights for improving energy efficiency in biomass systems.

Nomenclature

(continued)

A	Cross-sectional area of bond, m ²
c _k	Concentration of a certain type of particle in cell k
C _D	Drag coefficient
D _w	Cross-diffusion term
d _p	Diameter of spherical particles, m
E*	Equivalent Young's Modulus, Pa
E _i	Young's Modulus of sphere i, Pa
E _j	Young's Modulus of sphere j, Pa
F _{c,i}	Contact force acting on the sphere i, N
F _d	Drag force acting on the particles, N
F _n	Magnitude of the normal force, N
F _{d n}	Normal damping force, N
F _{n,ij}	Magnitude of the normal force between the spheres i and j, N
F _t	Magnitude of the tangential force, N
F _{d t}	Tangential damping force, N
g	Gravitational acceleration
G*	Equivalent shear modulus, Pa

(continued on next column)

G _k	Turbulent kinetic energy produced by the mean velocity gradient
G _ω	Production term of the specific dissipation rate
h	Total area of the drum
h _c	Heat conduction transfer coefficient
H	Particle proportion in the drum
I _i	Moment of inertia of sphere i, kg m ²
J	Moment of inertia, m ⁴
k	Turbulence kinetic energy
l ₁	Proportion of green particles
l ₂	Proportion of red particles
m	Mass of particle, kg
m _i	Mass of sphere i, kg
m _j	Mass of sphere j, kg
m*	Equivalent mass, kg
M	Lacey mixing index
M _{c,i}	Contact moment of sphere i
M _n	Normal torque between particles, N m
M _t	Tangential torque between particles, N m

(continued on next page)

* Corresponding author.

E-mail address: guconghuigch@163.com (C. Gu).

(continued)

N	Number of cells
$Nu_{p,i}$	Nusselt number of the particle
n	Number of lifters
n_p	Average number of particles within the cells
P_f	Fluid pressure, Pa
r^*	Geometric mean of the particle radii, m
R^*	Equivalent radius, m
R_B	The bonding radius, m
Re_p	Particle Reynolds number
R_i	Radius of sphere i, m
S_n	Normal stiffness, N m ⁻³
S_t	Tangential stiffness, N m ⁻³
S	Gas-solid momentum exchange source term
$S_{p,i}$	Surface area of the particle, m ²
S_k	Source terms of k
S_ω	Source terms of ω
T_p	Particle temperature, K
$T_{f,i}$	Fluid temperature, K
\mathbf{u}_f	Fluid velocity, m s ⁻¹
v_n^{rel}	Normal component of the relative velocity, m s ⁻¹
v_t^{rel}	Tangential component of the relative velocity, m s ⁻¹
v_i	Velocity of sphere i, m s ⁻¹
v_j	Velocity of sphere j, m s ⁻¹
v_n	Particle normal velocity, m s ⁻¹
v_p	Particle velocity, m s ⁻¹
V_c	Volume of the current grid cell, m ³
y	Distance to the next surface, m
Y_k	Dissipation of k
Y_ω	Dissipation of ω
Greek symbols	
β	Damping coefficient
μ_f	Fluid shear viscosity, Pa s
μ_r	Rolling friction coefficient
δ_n	Normal overlap of two adjacent spheres, m
δt	Time step, s
δ_t	Tangential overlap of two adjacent spheres, m
δ_{ij}	Kronecker delta symbol
σ_{\max}	Maximum normal shear stress, N
σ_k	Turbulence Prandtl numbers for k
σ_ω	Turbulence Prandtl numbers for ω
τ_{\max}	Maximum tangential shear stress, N
τ_f	Viscous stress tensor for a Newtonian fluid
ω	Rotational speed of the drum, r min ⁻¹
ω_{rel}	Unit vector of relative angular velocity
ω_n	Normal angular velocity, rad s ⁻¹
ω_t	Tangential angular velocity, rad s ⁻¹
ω_i	Angular velocity of particle i
ε_f	Mesh porosity
ρ_f	Fluid density, kg m ⁻³
λ_f	Fluid bulk viscosity, Pa s
Γ_k	effective diffusion rates of k
Γ_ω	effective diffusion rates of ω
$\kappa_{p,ij}$	Thermal conductivity of the particles, W (m K) ⁻¹
κ_f	Fluid thermal conductivity, W (m K) ⁻¹
Subscripts	
B	bonding
c	contact force
i	particle i
j	particle j
n	normal
p	particle
t	tangential

1. Introduction

As global demand for sustainable energy continues to grow, biomass energy is playing an increasingly important role in the transition of energy structures (Liu et al., 2023; Peukert & Bück, 2024). It can be directly used for combustion-based power and heat generation, and can also be converted into biofuels and biogas through thermochemical routes such as pyrolysis and gasification (Cho & Kong, 2025; Zhu et al., 2025). Before thermal conversion, wet biomass typically undergoes a drying pretreatment process to improve energy efficiency, enhance product quality, and reduce pollutant emissions (Kumar et al., 2022;

Wang et al., 2021). However, the energy efficiency of existing drying systems remains generally low, and operational costs are high, particularly when processing plant-based biomass particles with loose structures and highly variable moisture content. In such cases, uneven heat distribution frequently leads to poor drying quality and undermines overall system performance (Du et al., 2024; Gu et al., 2019; Moreno et al., 2016; Zhao et al., 2024).

In industrial applications, conventional biomass drying technologies often encounter issues such as low thermal efficiency, poor drying uniformity, and high operating costs, especially when handling plant-derived particles with high moisture content and porous structures. Specifically, thermal energy is difficult to distribute evenly within the particle interiors, resulting in over-drying or under-drying in certain regions, which subsequently impairs the efficiency of downstream thermal conversion and deteriorates the product quality. Furthermore, because of differences in heat transfer mechanisms and equipment structure, these systems exhibit significant variations in energy consumption per unit of moisture removal (Del Giudice et al., 2019; Yi et al., 2020).

To provide a clearer overview of the characteristics of mainstream drying technologies, Table 1 summarises six common drying methods, along with their heating sources and typical energy consumption ranges (Amos, 1999; Del Giudice et al., 2019; Havlík & Dlouhý, 2020; Murugan et al., 2021; Rashid et al., 2022; Rybak et al., 2021). Among these, rotary drum dryers demonstrate notable advantages in terms of energy efficiency. Their simple structure, operational stability, and suitability for continuous processing of bulk particulate materials have led to their widespread adoption in biomass drying applications.

In rotary drum drying systems, particles are subjected to complex motion behaviours such as sliding, rolling, and cascading, driven by the combined effects of gravity and mechanical forces. Structural parameters-such as drum rotation speed, internal baffle configuration, and wall temperature-directly influence the mixing state and thermal contact conditions of the particles (Adepu, Boepple, et al., 2021; Ardalaní et al., 2022, 2024; Seidenbecher et al., 2021). Existing studies have shown that increasing the rotational speed enhances the frequency of instantaneous contacts between particles and with the drum wall, which facilitates heat transfer (Hou et al., 2024; Xie et al., 2018). However, excessive speeds may reduce particle residence time in high-temperature zones, thus limiting thermal accumulation (Bheda et al., 2025; Chou et al., 2025; Jian et al., 2024; Jiang et al., 2024). The baffle structure disrupts particle accumulation, promoting spatial redistribution and agitation, which enhances mixing uniformity and heat transfer performance (Gu et al., 2025; Scherer et al., 2016; Xie et al., 2017). Meanwhile, the wall temperature governs the thermal driving force per unit time, playing a critical role in determining the particle heating rate and surface temperature distribution (Gu et al., 2019).

In practice, flexible biomass particles with high aspect ratios present significant uncertainty in their motion trajectories due to their non-

Table 1
Biomass drying techniques and their energy consumption characteristics.

Drying method	Heating source	Typical energy consumption (MJ kg ⁻¹ H ₂ O)	Reference
Hot air drying	Hot air	2.5–5.0	Amos (1999)
Rotary drum drying	Direct or indirect heat	1.4–3.5	Del Giudice et al. (2019)
Fluidised bed drying	Hot air, steam	1.3–3.2	Rashid et al. (2022)
Belt drying	Hot air, waste heat	2.0–4.0	Murugan et al. (2021)
Microwave drying	Microwave energy	1.0–2.5	Rybak et al. (2021)
Superheated steam drying	Superheated steam	2.8–4.5	Havlík and Dlouhý (2020)

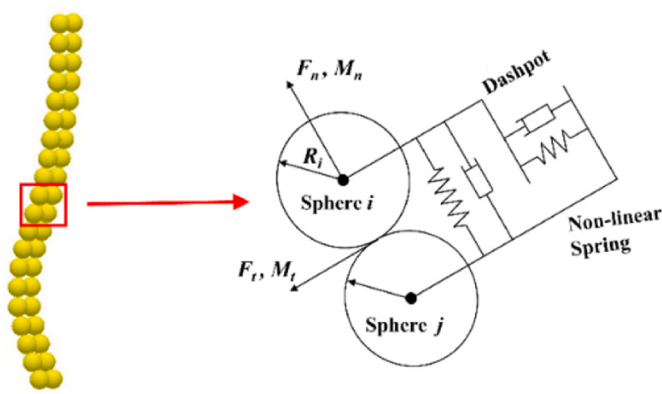


Fig. 1. Diagram of double-row-ball chain particle model.

spherical shapes and structural deformability (Deng et al., 2025). These particles tend to entangle, overlap, and agglomerate during drum rotation, thereby breaking the continuity of thermal contact paths in both spatial and temporal dimensions. This leads to pronounced non-uniformities in heat transfer and introduces considerable instability into the thermal conduction process (Wei et al., 2020). Traditional experimental approaches often struggle to capture essential parameters such as internal particle temperature distribution, heat flux variation, and contact evolution. The challenge becomes particularly severe under high temperatures, rapid drum rotation, complex multi-particle interactions, and irregularly shaped particles, where system disturbance and limited measurement precision are major obstacles (Gao et al., 2020; Park et al., 2024; Zare & Hashemabadi, 2019).

Against this backdrop, coupled Computational Fluid Dynamics-Discrete Element Method (CFD-DEM) modelling has emerged as a powerful tool for analysing multiscale heat transfer in particulate systems (Chen et al., 2022; Morimoto et al., 2023; Schirck & Morris, 2024a, 2024b; Wang et al., 2024a; Washino et al., 2023). This approach enables the simultaneous resolution of fluid flow and particle dynamics, while allowing for detailed modelling of individual particles to capture microscopic behaviours such as deformation, rotation, and contact evolution (Fei et al., 2025; Fischer et al., 2023; Illana et al., 2024; Ma et al., 2022). In recent years, modelling methods for fibre-like non-spherical particles have advanced considerably, incorporating diverse structural representations and contact modelling strategies to more accurately simulate particle deformation and multi-point contact behaviour (Kildashti et al., 2023; Romero-Valle et al., 2021; Ullah et al., 2019; Wang et al., 2024b; Wang et al., 2024c; Zhu et al., 2021). Nevertheless, systematic modelling and multiparameter analysis of high aspect-ratio biomass particles in rotary drums remain limited, particularly regarding the evolution of mixing states, local temperature rise mechanisms, and control of heat transfer efficiency (Han et al., 2023; Saruwatari & Nakamura, 2022; Tsotsas, 2019).

In addition, insufficient attention has been given to how unsteady heat transfer affects the quality of biomass drying. Variations in heating rate and local thermal accumulation can induce structural denaturation and spatial mismatch of pyrolysis zones, thereby altering combustion performance and affecting the yield and composition of conversion products (Kuznetsov et al., 2021; Qurat-ul-Ain et al., 2021). Therefore, understanding how drum structural parameters influence particle mixing behaviour and thermal evolution is crucial for achieving more uniform heat transfer, enhancing drying efficiency, and improving product quality.

In this study, flexible, high aspect-ratio fibre-like tobacco leaf particles were selected as representative biomass. Tobacco leaves, as a typical form of non-spherical plant-based biomass, exhibit structural morphology and thermal responses that are broadly representative of other fibrous particles. The model systematically examines how

variations in drum rotation speed, baffle number, and wall temperature affect particle motion and temperature evolution. The Lacey mixing index is introduced to quantitatively evaluate the degree of mixing, thereby revealing the coupled relationship between mixing uniformity and heat transfer efficiency. The findings contribute to a deeper understanding of heat transfer mechanisms in dynamic drying processes involving high aspect-ratio biomass and provide theoretical support and modelling guidance for the structural optimisation and operational design of flexible particle-based thermal treatment systems.

2. Numerical methods

2.1. Model descriptions

This study employs CFD-DEM to simulate the flow mixing and heat transfer processes of deformable high aspect-ratio particles in a rotary drum. The gas phase is resolved using the Navier-Stokes equations, while the particle phase is tracked with a Lagrangian approach to obtain particle trajectories. Interactions between gas and particles, the influence of turbulence on inter-particle interactions, and particle-wall collisions are considered. The heat transfer mechanisms include direct conduction between particles, convective heat transfer between particles and gas, and radiative heat transfer between particles and the surrounding fluid or other particles.

2.2. Mathematical model

To accurately represent the deformation, contact, and packing behaviour of biomass particles in the rotary drum, a discrete element model for deformable high aspect-ratio particles was established in this section. This model is based on the typical structural features of biomass materials, such as high flexibility, slender geometry, and ease of deformation. A double-row ball chain structure was adopted to reflect these physical characteristics, thereby providing a mechanical basis for subsequent simulations of mixing and heat transfer.

The model has a length of 10 mm, a width of 1 mm, and a thickness of 0.5 mm. Each particle consists of a double row of 2×20 small spheres with a diameter of 0.5 mm. Virtual bonds are added between adjacent spheres, bonding them into a chain-like structure. These bonds constrain the relative displacement and rotation of the spheres in all axes by transmitting normal and tangential forces as well as bending and torsional moments. The bonding effect is equivalent to a set of nonlinear springs, restricting movement in multiple directions, as shown in Fig. 1.

Within a single time step, the forces and moments between each set of springs are calculated according to the following equations (Potyondy & Cundall, 2004):

$$\delta F_n = -v_n S_n A \delta t \quad (1)$$

$$\delta F_t = -v_t S_t A \delta t \quad (2)$$

$$\delta M_n = -\omega_n S_t J \delta t \quad (3)$$

$$\delta M_t = -\omega_t S_n \frac{J}{2} \delta t \quad (4)$$

where, δt is the time step, v_n is the normal velocity, v_t is the tangential velocity, ω_n is the normal angular velocity, ω_t is the tangential angular velocity, S_n is the normal stiffness, S_t is the tangential stiffness, F_n is the normal bonding force, F_t is the tangential bonding force, M_n is the normal moment, M_t is the tangential moment, A is the contact area, R_B is the bonding radius, and J is the moment of inertia.

When the normal and tangential shear stresses reach their limit values, the bonding bonds break:

$$\sigma_{\max} < -\frac{F_n}{A} + \frac{2M_t}{J} R_B \quad (5)$$

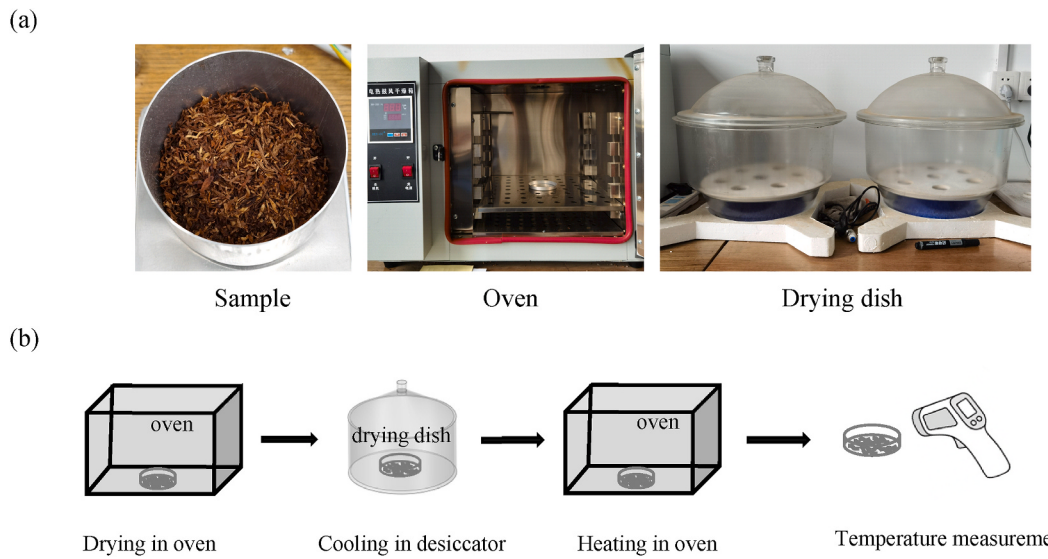


Fig. 2. (a) The experimental materials; (b) Pictorial of the setup.

Table 2
Physical properties of the particles.

Parameters	Values
Mass, g	0.075 ± 0.0075
Length, mm	10 ± 5
Width, mm	1 ± 0.1
Thickness, mm	0.5 ± 0.2
Density, kg m^{-3}	1065

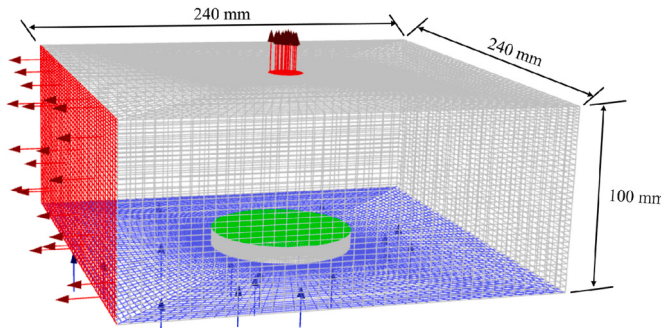


Fig. 3. The geometry and mesh of the air-blast drying box.

$$\tau_{\max} < -\frac{F_t}{A} + \frac{2M_n}{J}R_B \quad (6)$$

where, σ_{\max} is the normal critical shear stress, and τ_{\max} is the tangential critical shear stress.

The normal elastic force and normal damping force between particles or between particles and geometric structures are calculated as follows (Huang et al., 2021; Nassauer & Kuna, 2013):

$$F_n = \frac{4}{3}E^* \sqrt{R^*} \delta_n^3 \quad (7)$$

$$F_n^d = -2\sqrt{\frac{5}{6}}\beta\sqrt{S_n}m^*v_n^{rel} \quad (8)$$

$$\frac{1}{E^*} = \frac{(1 - v_i^2)}{E_i} + \frac{(1 - v_j^2)}{E_j} \quad (9)$$

Table 3
Parameters of validation simulation.

Parameters	Values
Inlet air velocity, m s^{-1}	0.5
Inlet air Temperature, K	323.15, 333.15, 343.15
Inlet Turbulence Intensity, %	5
Inlet Hydraulic Diameter, mm	160
Left Outlet Turbulence Intensity, %	5
Left outlet hydraulic diameter, mm	141.18
Left outlet recirculation temperature, K	323.15, 333.15, 343.15
Upper outlet turbulence intensity, %	5
Upper outlet hydraulic diameter, mm	40
Upper outlet recirculation temperature, K	300
Aluminium lid density, kg m^{-3}	2700
Aluminium lid Young's modulus, Pa	7.17×10^{10}
Aluminium lid Poisson's ratio	0.33
Aluminium lid thermal conductivity, $\text{W m}^{-1} \text{K}^{-1}$	236
Aluminium lid specific heat capacity, $\text{J kg}^{-1} \text{K}^{-1}$	902
Aluminium lid wall temperature, K	323.15, 333.15, 343.15
Particle mass, g	2.665, 2.669, 2.700
Particle initial temperature, K	291.62, 291.18, 291.25
Gas phase time step size, s	4×10^{-5}
Solid phase time step size, s	4×10^{-6}

$$\frac{1}{R^*} = \frac{1}{R_i} + \frac{1}{R_j} \quad (10)$$

$$\beta = \frac{-\ln e}{\sqrt{\ln^2 e + \pi^2}} \quad (11)$$

$$S_n = 2E^* \sqrt{R^*} \delta_n \quad (12)$$

$$m^* = \left(\frac{1}{m_i} + \frac{1}{m_j} \right)^{-1} \quad (13)$$

where, E^* is the effective Young's modulus, R^* is the effective radius, δ_n is the normal contact deformation, β is the damping coefficient, S_n is the normal stiffness, m^* is the effective mass, v_n^{rel} is the normal relative velocity, E_i and E_j are the Young's moduli, v_i and v_j are the Poisson ratios, R_i and R_j are the radii of the spheres, and m_i and m_j are the masses of the spheres.

The tangential elastic force and tangential damping force are calculated as follows (Mindlin & Deresiewicz, 1953):

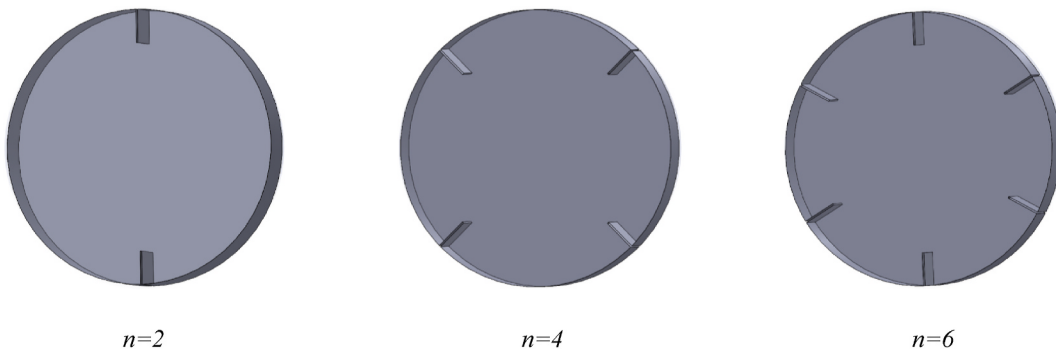


Fig. 4. Grid model of the drum for three different numbers of baffles.

Table 4
Parameters of particle model.

Category	Parameters	Values
Particles	Density, $\text{kg}\cdot\text{m}^{-3}$	7930
	Young's modulus, Pa	1.93×10^{11}
	Poisson's ratio	0.3
	Density, $\text{kg}\cdot\text{m}^{-3}$	1065
Contact parameters	Young's modulus, Pa	9.4×10^6
	Poisson's ratio	0.3
	The friction coefficient of particle-particle	0.1
	The static friction coefficient of particle-particle	0.3
Contact parameters	The rolling friction coefficient of particle-particle	0.01
	The rolling friction coefficient of particle-particle	0.01
	The friction coefficient of particle-wall	0.2
	The static friction coefficient of particle-wall	0.2
	The rolling friction coefficient of particle-wall	0.01

Table 5
Parameters of heat transfer simulation.

Parameters	Values
Inlet air velocity, $\text{m}\cdot\text{s}^{-1}$	0.3
Inlet temperature, K	343.15
Inlet turbulence intensity, %	5
Inlet hydraulic diameter, mm	170
Outlet turbulence intensity, %	5
Outlet hydraulic diameter, mm	170
Outlet recirculation temperature, K	343.15
Particle thermal conductivity, $\text{W}\cdot\text{m}^{-1}\cdot\text{K}^{-1}$	0.128
Particle specific heat capacity, $\text{J}\cdot\text{kg}^{-1}\cdot\text{K}^{-1}$	1000
Particle initial temperature, K	298.15
Number of particles	4150
Rotary drum thermal conductivity, $\text{W}\cdot\text{m}^{-1}\cdot\text{K}^{-1}$	16.3
Rotary drum specific heat capacity, $\text{J}\cdot\text{kg}^{-1}\cdot\text{K}^{-1}$	500
Rotary drum wall temperature, K	343.15, 373.15, 403.15
Rotary drum rotational speed, r min^{-1}	6, 8, 10, 12
Gas phase time step, s	5×10^{-5}
Solid phase time step, s	5×10^{-6}

$$F_t = -S_t \delta_t \quad (14)$$

$$F_t^d = -2\sqrt{\frac{5}{6}}b\sqrt{S_t m^* v_t^* \vec{v}_{rel}} \quad (15)$$

$$S_t = 8G^* \sqrt{R^* \delta_t} \quad (16)$$

where, S_t is the tangential stiffness, δ_t is the tangential contact deformation, \vec{v}_{rel} is the tangential relative velocity, and G^* is the effective shear modulus.

The rolling friction of the double-row ball chain particles is modelled based on the Contact Independent Directional Constant Torque Model,

and the torque applied to the surface of the spheres is calculated as follows (Sakaguchi et al., 1993):

$$\tau_i = -\mu_r F_n R_i \omega_i \quad (17)$$

where, μ_r is the rolling friction coefficient of the spheres, F_n is the normal contact force on the sphere surface, R_i is the distance between the contact point and the centre of mass, and ω_i is the unit angular velocity vector at the contact point of the sphere.

The equation of motion for the particle model can be described as (Ai et al., 2011):

$$m_i \frac{dv_i}{dt} = \sum F_{c,i} + F_{d,i} + m_i g \quad (18)$$

$$\frac{d(I_i \omega_i)}{dt} = \sum M_{c,i} - \mu_r F_{n,ij} R_i^* \omega_{rel,i} \quad (19)$$

where, t is the time, m_i is the particle mass, v_i is the particle linear velocity, $F_{c,i}$ is the contact force between particles, $F_{d,i}$ is the drag force on the particle, I_i is the moment of inertia, ω_i is the angular velocity of the particle, $M_{c,i}$ is the contact moment, μ_r is the rolling friction coefficient, $F_{n,ij}$ is the normal contact force, R_i^* is the effective radius, and $\omega_{rel,i}$ is the relative unit angular velocity vector.

2.3. Gas-solid two phases control equations

The CFD-DEM coupling method, within the Eulerian framework, solves the fluid motion based on the continuum assumption using the classical Navier-Stokes governing equations. The mass conservation equation and momentum conservation equation for the fluid are (Pan et al., 2016):

$$\frac{\partial}{\partial t} (\epsilon_f \rho_f) + \frac{\partial}{\partial x_i} (\epsilon_f \rho_f u_{f,i}) = 0 \quad (20)$$

$$\frac{\partial}{\partial t} (\epsilon_f \rho_f \mathbf{u}_{f,i}) + \frac{\partial}{\partial x_j} (\epsilon_f \rho_f \mathbf{u}_{f,i} \mathbf{u}_{f,j}) = -\epsilon_f \frac{\partial p_f}{\partial x_i} + \epsilon_f \rho_f \mathbf{g} + \frac{\partial}{\partial x_j} (\epsilon_f \tau_f) - \mathbf{S} \quad (21)$$

where, ϵ_f is the mesh porosity, ρ_f is the fluid density, \mathbf{u}_f is the fluid velocity, p_f is the fluid pressure, \mathbf{g} is the gravitational acceleration, and \mathbf{S} is the gas-solid momentum exchange source term. The τ_f is the viscous stress tensor for a Newtonian fluid, given by (Versteeg and Malalasekera, 2007):

$$\tau_f = \mu_f \left(\frac{\partial \mathbf{u}_{f,i}}{\partial x_j} + \frac{\partial \mathbf{u}_{f,j}}{\partial x_i} \right) + \left(\lambda_f - \frac{2}{3} \mu_f \right) \frac{\partial \mathbf{u}_{f,k}}{\partial x_j} \delta_{ij} \quad (22)$$

where μ_f is the fluid shear viscosity, λ_f is the fluid bulk viscosity, and δ_{ij} is the Kronecker delta symbol. This study uses the SST $k-\omega$ model to compute the airflow within the rotary drum (Menter, 1994).

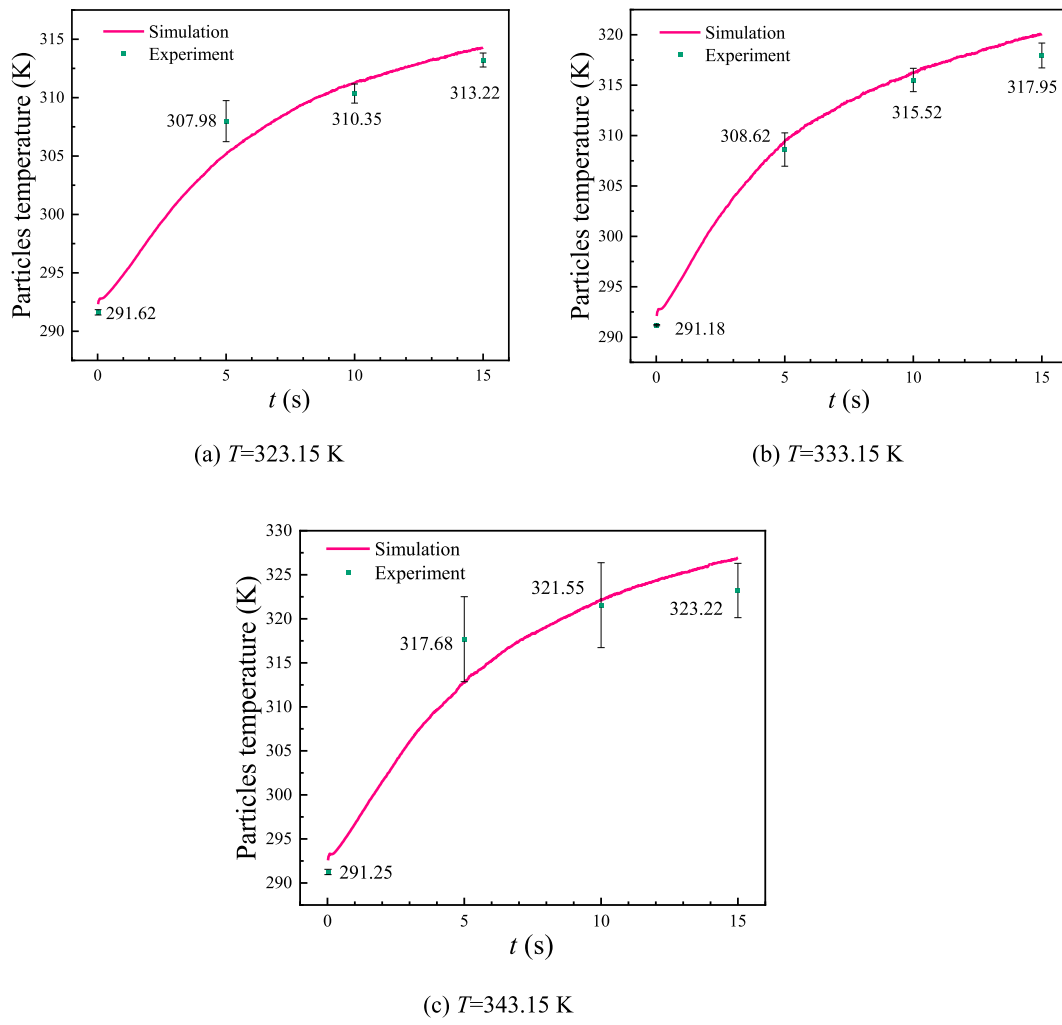


Fig. 5. Particles temperature variation over time: Simulation vs. Experiment.

$$\frac{\partial}{\partial t} (\rho_f k) + \frac{\partial}{\partial x_i} (\rho_f k u_i) = \frac{\partial}{\partial x_j} \left(\Gamma_k \frac{\partial k}{\partial x_j} \right) + G_k - Y_k + S_k + G_b \quad (23)$$

$$\frac{\partial}{\partial t} (\rho_f \omega) + \frac{\partial}{\partial x_i} (\rho_f \omega u_i) = \frac{\partial}{\partial x_j} \left(\Gamma_\omega \frac{\partial \omega}{\partial x_j} \right) + G_\omega - Y_\omega + D_\omega + S_\omega + G_{\omega b} \quad (24)$$

where, Γ_k and Γ_ω are the effective diffusion rates of k and ω , respectively; G_k is the turbulent kinetic energy produced by the mean velocity gradient; G_ω is the production term of the specific dissipation rate; Y_k and Y_ω are the dissipation of k and ω due to turbulence, respectively; S_k and S_ω are source terms; D_ω is the cross-diffusion term; and G_b and $G_{\omega b}$ are buoyancy terms.

The effective diffusion rates Γ_k and Γ_ω are calculated as follows (Menter, 1994):

$$\Gamma_k = \mu + \frac{\mu_t}{\sigma_k} \quad (25)$$

$$\Gamma_\omega = \mu + \frac{\mu_t}{\sigma_\omega} \quad (26)$$

where, σ_k and σ_ω are the turbulence Prandtl numbers for k and ω .

$$\sigma_k = \frac{1}{F_1/\sigma_{k,1} + (1-F_1)/\sigma_{k,2}} \quad (27)$$

$$\sigma_\omega = \frac{1}{F_1/\sigma_{\omega,1} + (1-F_1)/\sigma_{\omega,2}} \quad (28)$$

$$F_1 = \tanh(\Phi_1^4) \quad (29)$$

$$\Phi_1 = \min \left[\max \left(\frac{\sqrt{k}}{0.09\omega y}, \frac{500\mu}{\rho y^2 \omega} \right), \frac{4\rho k}{\sigma_{\omega,2} D_\omega^+ y^2} \right] \quad (30)$$

where, y is the distance to the next surface, and D_ω^+ is the positive part of the cross-diffusion term.

$$D_\omega^+ = \max \left[2\rho \frac{1}{\sigma_{\omega,2}} \frac{1}{\omega} \frac{\partial k}{\partial x_i} \frac{\partial \omega}{\partial x_j}, 10^{-10} \right] \quad (31)$$

$$G_k = -\rho \bar{u}_i' \bar{u}_j' \frac{\partial u_j}{\partial x_i} \quad (32)$$

$$G_\omega = \frac{\alpha \alpha^*}{v_t} G_k \quad (33)$$

$$Y_k = \rho \beta^* k \omega \quad (34)$$

$$Y_\omega = \rho \beta \omega^2 \quad (35)$$

$$D_\omega = 2(1-F_1)\rho \frac{1}{\omega \sigma_{\omega,2}} \frac{\partial k}{\partial x_j} \frac{\partial \omega}{\partial x_j} \quad (36)$$

The limiter for the turbulent viscosity equation in the SST model (Menter, 1994) is given by: $\mu_t = \frac{\rho k}{\omega} \frac{1}{\max \left[\frac{1}{\alpha^*} \frac{S F_2}{\sigma_{\omega,1} \omega} \right]} \quad (37)$

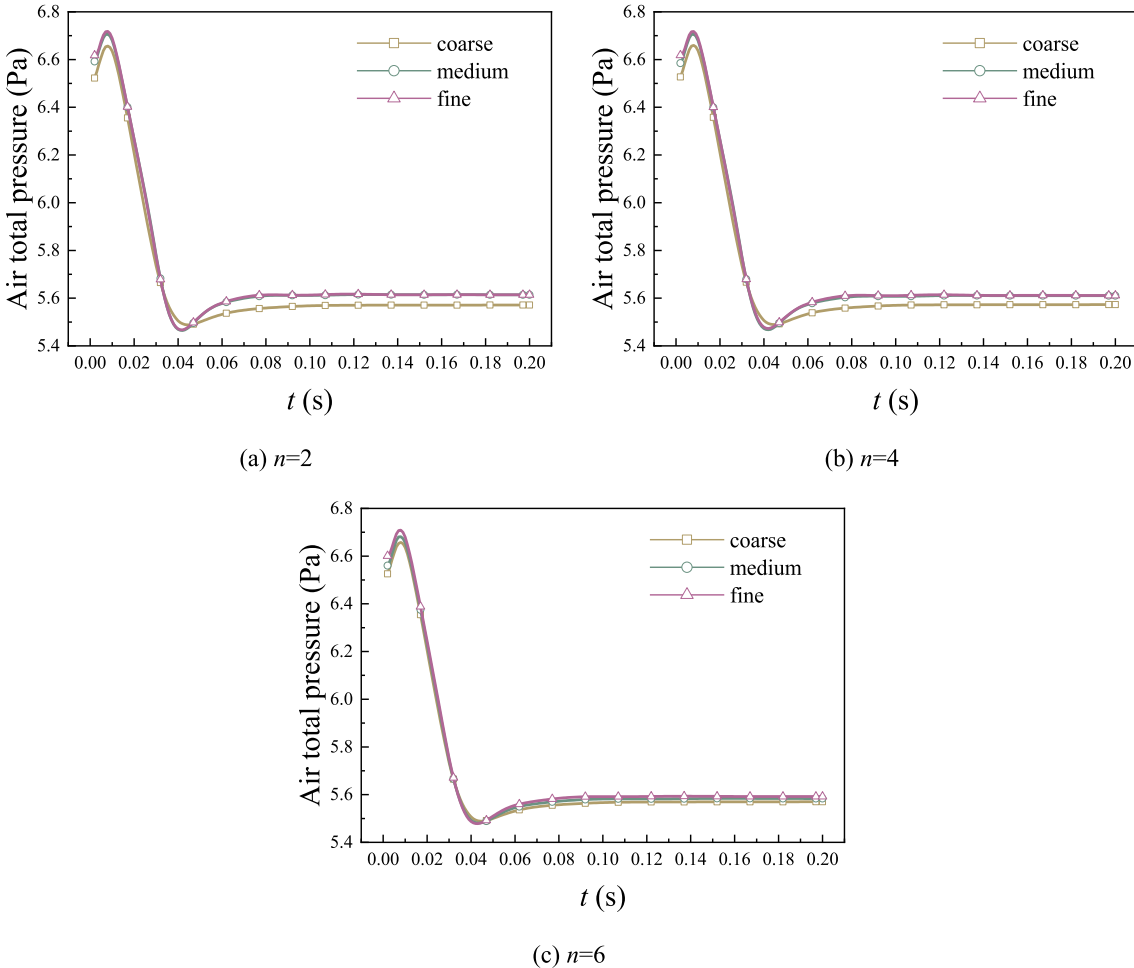


Fig. 6. Air total pressure variation over time for different grid densities: (a) $n = 2$; (b) $n = 4$; (c) $n = 6$. The three grid resolutions correspond to coarse (65,674), medium (126,928), and fine (197,311).

Where, \mathbf{S} is the magnitude of the strain rate, and F_2 is calculated as:

$$F_2 = \tanh(\phi_2^2) \quad (38)$$

$$\phi_2 = \max\left(2 \frac{\sqrt{k}}{0.09\omega}, \frac{500\mu}{\rho y^2\omega}\right) \quad (39)$$

The model constants in the above equations (Menter, 1994) are as follows:

$$\sigma_{k,1} = 1.176; \sigma_{k,1} = 2.0; \sigma_{\omega,1} = 1.0; \sigma_{\omega,2} = 1.168;$$

$$a_1 = 0.31; \beta_{i,1} = 0.075; \beta_{i,1} = 0.0828$$

In CFD-DEM coupled simulations, the momentum exchange between particles and the fluid is primarily represented by drag forces. When the deformable high aspect-ratio particles move in the rotary drum, they are also affected by drag forces from the airflow. Ignoring other negligible forces, the gas-solid momentum exchange source term \mathbf{S} in the gas phase governing equations can be calculated as follows (Deen et al., 2007):

$$\mathbf{S} = \frac{1}{V_c} \sum_{i=1}^{n_p} F_d \quad (40)$$

where n_p is the number of particles in the current grid, V_c is the volume of the current grid cell, and F_d is the drag force acting on the particles. In the gas-solid coupling process, the drag force on the double-row ball chain particles is the vector sum of the drag forces on all the spheres. Therefore, the drag force model used is based on the spherical particle

Morsi-Alexander model. The drag force acting on the deformable high aspect-ratio particles is calculated as follows (Morsi & Alexander, 1972):

$$F_d = \frac{1}{2} \rho_f \varepsilon_f^2 C_D A_p |\mathbf{u}_f - \mathbf{v}_p| (\mathbf{u}_f - \mathbf{v}_p) \quad (41)$$

$$C_D = a_1 + \frac{a_2}{Re} + \frac{a_3}{Re^2} \quad (42)$$

$$a_1, a_2, a_3 = \begin{cases} 0, 24, 0 & 0 < Re < 0.1 \\ 3.690, 22.73, 0.0903 & 0.1 < Re < 1 \\ 1.222, 29.1667, -3.8889 & 1 < Re < 10 \\ 0.6167, 46.50, -116.67 & 10 < Re < 100 \\ 0.3644, 98.33, -2778 & 100 < Re < 1000 \\ 0.357, 148.62, -47500 & 1000 < Re < 5000 \\ 0.46, -490.546, 578700 & 5000 < Re < 10000 \\ 0.5191, -1662.5, 5416700 & Re \geq 10000 \end{cases} \quad (43)$$

$$Re_p = \frac{\varepsilon_f \rho_f |\mathbf{u}_f - \mathbf{v}_p| d_p}{\mu_f} \quad (44)$$

where, C_D is the drag coefficient, A_p is the projected area of the particle in the direction of flow, \mathbf{u}_f is the fluid velocity, and \mathbf{v}_p is the particle velocity, Re_p is the particle Reynolds number and d_p is the diameter of the sphere.

2.4. Heat transfer model

There are three modes of heat transfer: conduction, convection, and

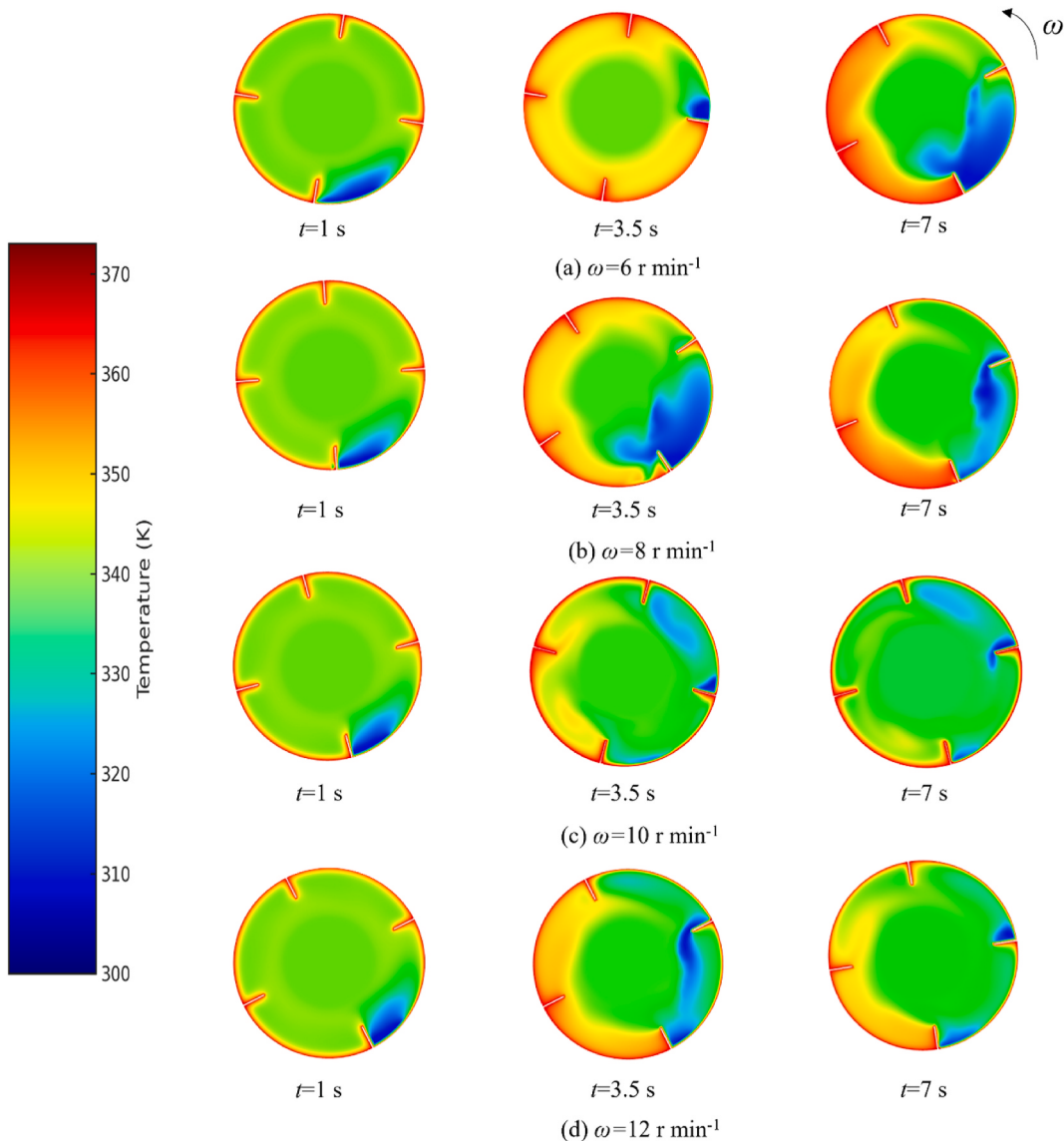


Fig. 7. Simulated temperature contours of particles at different drum rotation speeds and time points.

radiation. During heating of the particles in the rotary drum, the heat transfer is primarily composed of conduction between particles, conduction between particles and the wall, and convective heat transfer between particles and the airflow. For temperatures below 673.15 K, the radiative heat transfer between the particles and the wall can be neglected (Asakuma, 2013). Therefore, this study only considers heat conduction and convection.

Based on the temperature difference and the overlap of collisions between particles, the conductive heat transfer between particles can be calculated as (Chaudhuri et al., 2006):

$$Q_{pp,ij} = k_c (T_{pj} - T_{pi}) \quad (45)$$

$$k_c = \frac{4\kappa_{pi}\kappa_{pj}}{\kappa_{pi} + \kappa_{pj}} \left(\frac{3F_N r^*}{4E} \right)^{1/3} \quad (46)$$

where, T_{pi} denotes the temperature difference between particle i and particle j , and i and j refer to a pair of particles in contact, k_c is the heat conduction transfer coefficient, κ_{pi} is the thermal conductivity of the particles, F_N is the normal force, r^* is the geometric mean of the particle radii based on Hertzian contact theory, and E is the effective Young's modulus of the particles. The terms inside the parentheses on the right-

hand side calculate the contact radius between the particles and the wall/other particles.

When the particles move and tumble inside the rotary drum, they will undergo convective heat transfer with the hot air in the drum and at the drum inlet. The convective heat transfer follows Newton's cooling law. The convective heat transfer between the particles and the fluid is calculated as:

$$Q_{pf,i} = h_{pf,i} S_{pi} (T_{fi} - T_{pi}) \quad (47)$$

where, T_{fi} is the fluid temperature, T_{pi} is the particle temperature, S_{pi} is the surface area of the particle, and $h_{pf,i}$ is the convective heat transfer coefficient between the particle and the fluid. The convective heat transfer coefficient can be calculated using the Nusselt number as (Ranz and Marshall, 1952):

$$h_{pf,i} = Nu_{pi} \frac{\kappa_f}{d_{pi}} \quad (48)$$

$$Nu_{pi} = 2 + 0.6 Re^{1/2} Pr^{1/3} \quad (49)$$

where, Nu_{pi} is the Nusselt number of the particle, κ_f is the fluid thermal conductivity, and d_{pi} is the particle diameter.

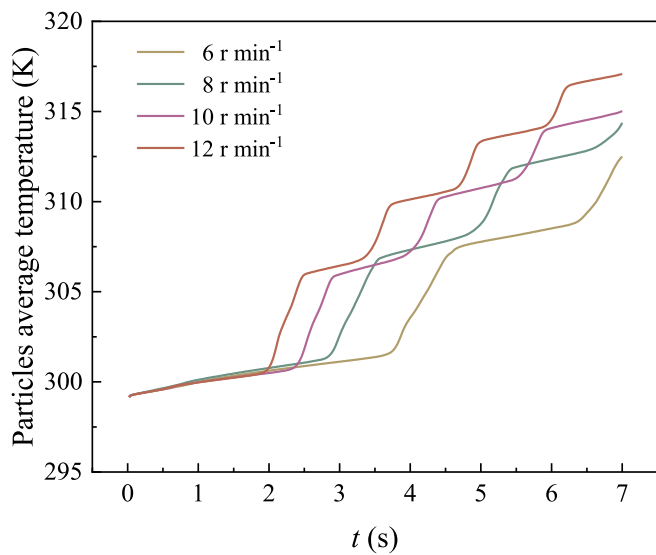


Fig. 8. Simulated results of variation in average particle temperature with time at different drum rotation speeds ($n = 4$).

Since this study uses non-spherical particles based on multi-sphere models, the convective heat transfer between each deformable high aspect-ratio particle and the fluid can be obtained by summing the

convective heat transfer from each sphere that constitutes the particle. Therefore, the calculation of the convective heat transfer coefficient is based on the Nusselt number and radius of the individual spheres. According to the conservation of energy, the heat entering the particle equals the sum of the conductive and convective heat transfer. Therefore, the temperature equation for the deformable high aspect-ratio particles can be written as (Zhou et al., 2023):

$$m_{p,i}c_p \frac{dT_p}{dt} = Q_{pp,ij} + Q_{fp,i} \quad (50)$$

where, $m_{p,i}$ is the particle mass, c_p is the specific heat capacity of the particle, and T_p is the particle temperature.

For the fluid phase, its temperature field is also solved using the energy conservation equation for the gas-solid two-phase coupling (Liu et al., 2022):

$$\frac{\partial}{\partial t} (\epsilon_f \rho_f c_{pf} T_f) + \nabla \cdot (\epsilon_f \rho_f c_{pf} T_f \mathbf{u}_f) = \nabla \cdot (\epsilon_f \kappa_f \nabla T_f) + \sum Q_{i,conv} \quad (51)$$

in the equation, the first term on the left-hand side represents the unsteady term, which indicates the change in internal energy within the control volume. The second term represents the convective term, which represents the heat passing through the control surface. On the right-hand side, the first term represents the diffusion term, which indicates the heat entering the control volume due to conduction within the fluid. The second term represents the gas-solid convection term, which indicates the heat exchanged between the particles and the fluid within

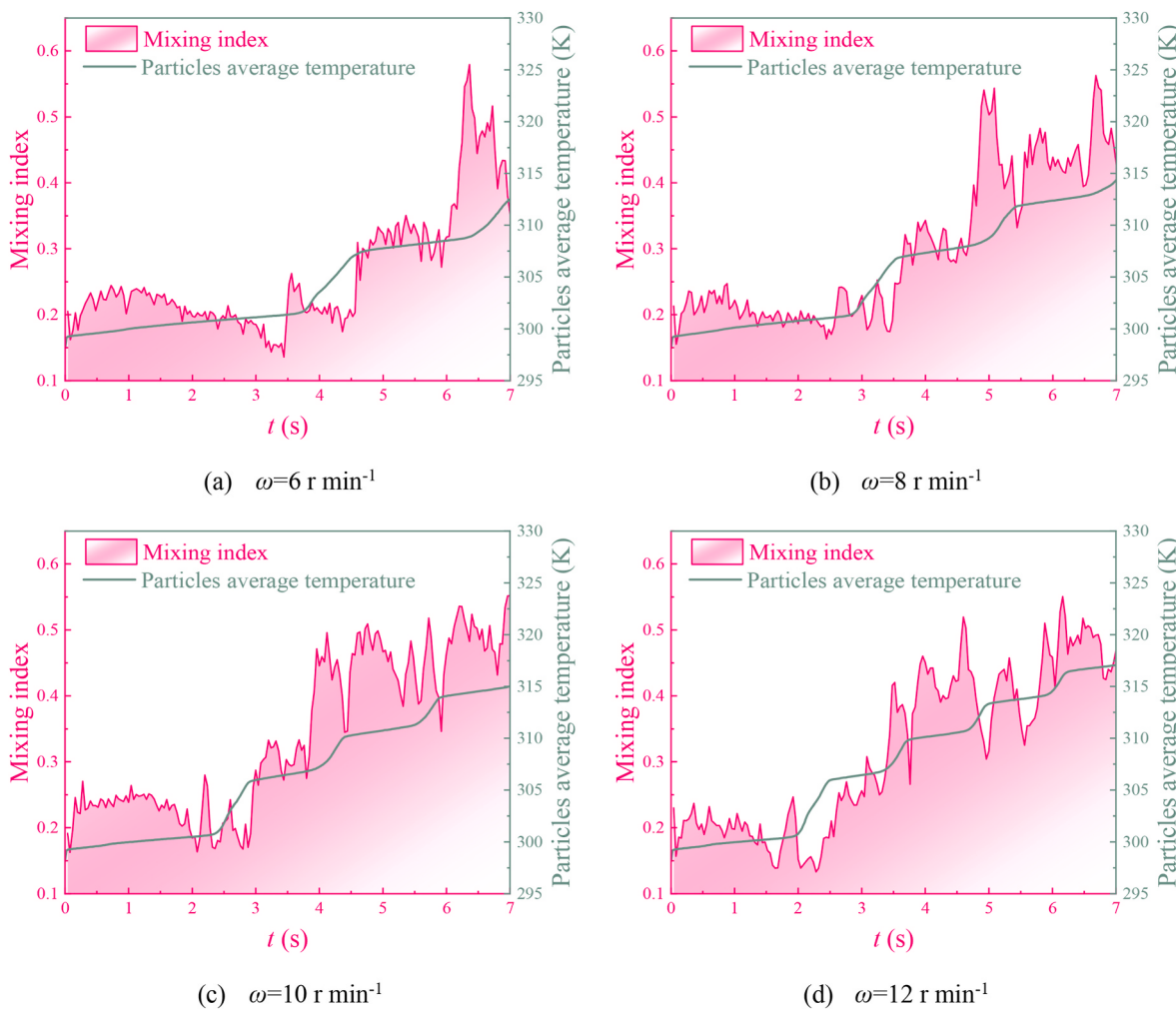


Fig. 9. Simulated results of variation in average particle temperature and mixing index with time at different drum rotation speeds.

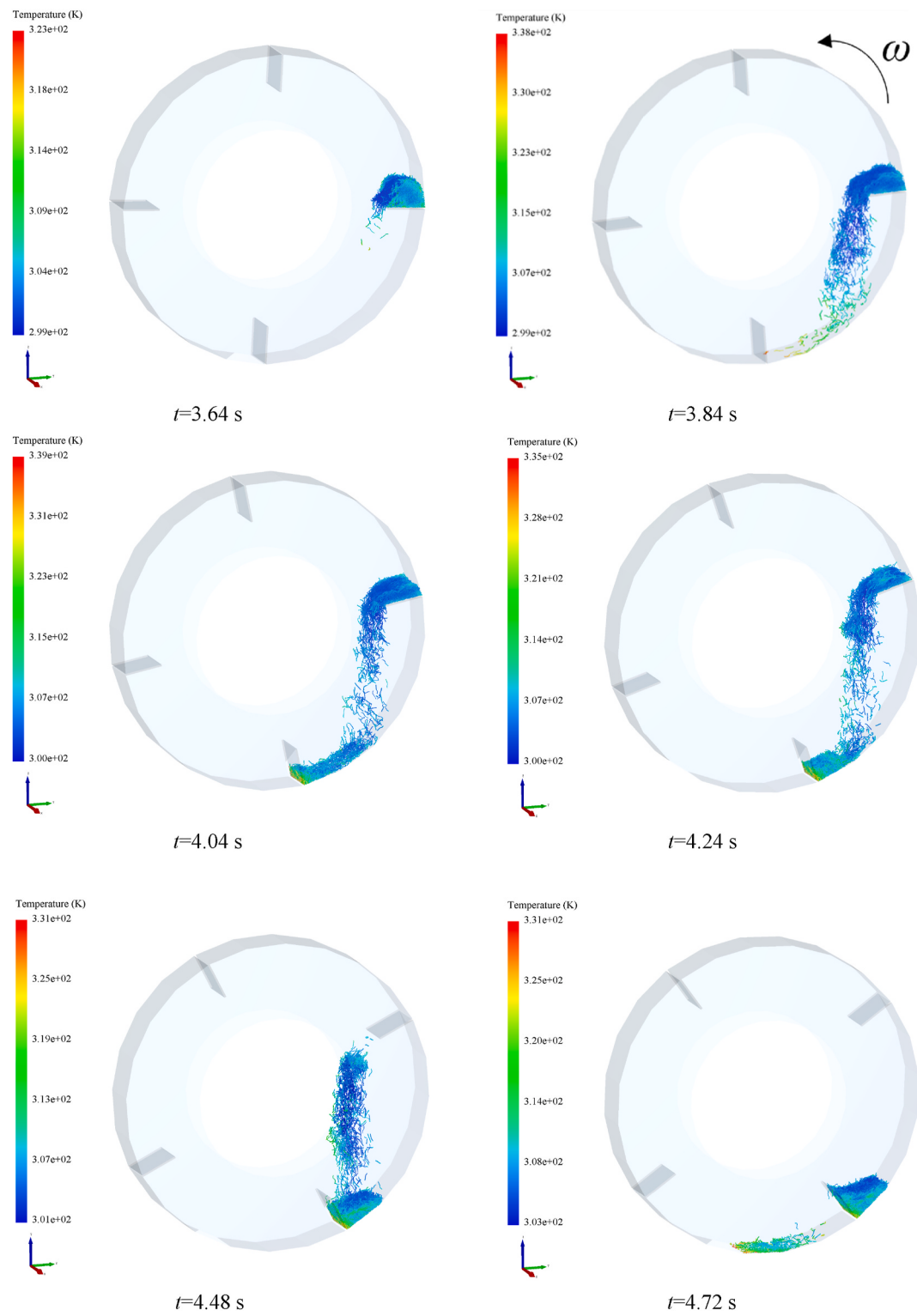


Fig. 10. Simulated results of the particle motion and heat transfer process in the drum ($n = 4$, $\omega = 6 \text{ r min}^{-1}$).

the control volume.

2.5. Experimental validation

To eliminate the influence of moisture content on the temperature of the fibres, absolutely dry fibres were prepared. The drying process is as follows: First, the temperature of the electric heating forced-air drying oven was set to 363.15 K. Equal masses of moist tobacco leaf fibres, each

with a weight of 20 g and an initial moisture content of approximately 16 %, were placed in aluminium boxes. The lids of the boxes were removed and the boxes were placed in the centre of the oven for 3 h of drying. Once all the moisture had evaporated from the fibres, the aluminium boxes were removed, closed, and transferred to a drying dish containing silica gel desiccant to cool to room temperature, preventing high temperatures from affecting the subsequent heating experiments. After this drying process, the moisture content of the fibres was reduced

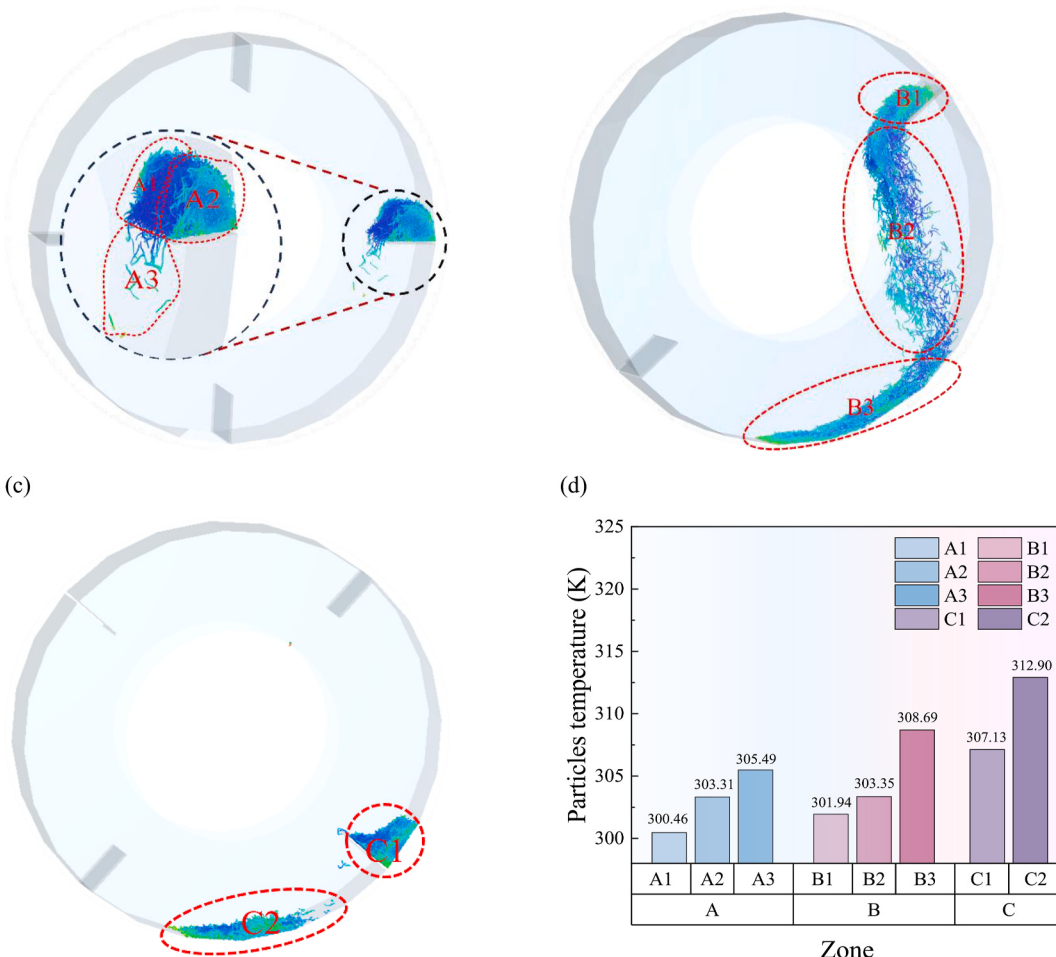


Fig. 11. (a–c) Division of the simulation image; (d) Average temperature of particles in different regions ($n = 4$, $\omega = 6 \text{ r min}^{-1}$).

to nearly zero. The experimental materials and pictorial of the setup are shown in Fig. 2. The basic physical characteristics of the biomass particles are listed in Table 2. The basic physical characteristics of the biomass particles are listed in Table 2. The particle mass was measured using a precision electronic balance, the length, width, and thickness were obtained by repeated measurements with a vernier calliper, and the density was calculated from the measured mass and geometric volume. For irregular shapes, the density was further verified using the liquid displacement method.

During the heat transfer experiment, the electric heating forced-air drying oven was first preheated to the experimental temperature. Once the oven reached and stabilised at the target temperature, the dried leaf-stem fibres were removed from the drying dish, and the initial temperature T_0 was recorded. The fibres were then placed at the centre of the aluminium box lid, which was positioned on the tray inside the drying oven. The oven door was closed, and the timer started. Every 5 s, the temperature at the centre of the fibre stack was measured using an infrared thermometer, and the temperature readings were recorded. Each set of experiments was repeated three times, with temperature measurements taken at 5 s, 10 s, and 15 s, denoted as T_5 , T_{10} , and T_{15} , respectively. The experiments were carried out at three different temperatures: 323.15 K, 333.15 K, and 343.15 K. Each temperature condition was repeated three times, and the average value was used to reduce experimental error.

To reduce the computational load in the CFD heat transfer model, the simulation domain was simplified by considering only the space above the trays in the drying chamber. The electric air-blast drying box had dimensions of 240 mm × 240 mm × 100 mm, while the aluminium lid

inside the drying box had a diameter of 80 mm and a height of 10 mm. Fig. 3 presents the geometry of the drying box and the mesh details. The chamber was discretised using hexahedral meshes. The average mesh quality was 0.9085, and the minimum mesh quality was 0.7065. The simulation adopted a CFD-DEM coupled method, with the bottom tray region set as the hot air velocity inlet, where the velocity was measured using a hot-wire anemometer. The left side and upper ventilation openings were set as pressure outlets, with the remaining surfaces as adiabatic walls. The turbulence model used is described in Section 2.3. For the particle phase, deformable high aspect-ratio particles with the same mass and initial temperature as in the experiments were generated at the centre of the flow field at the bottom, at the location of the aluminium lid. Other simulation parameters, initial conditions, and boundary conditions are shown in Table 3. These parameters are consistent with the experimental conditions. Boundary inputs such as air velocity, temperature, and turbulence intensity were based on the experimental setup, while the material properties of the aluminium lid were adopted as typical values commonly used in numerical simulations.

2.6. Grid independence verification

To study the heat transfer characteristics of deformable high aspect-ratio particles during their motion in the rotary drum, hexahedral meshes were generated for drums with baffle counts of $n = 2$, 4, and 6. To ensure the accuracy of the numerical simulation, a grid density sensitivity analysis was conducted. For each drum, three mesh models with grid sizes ranging from small to large were generated, with the

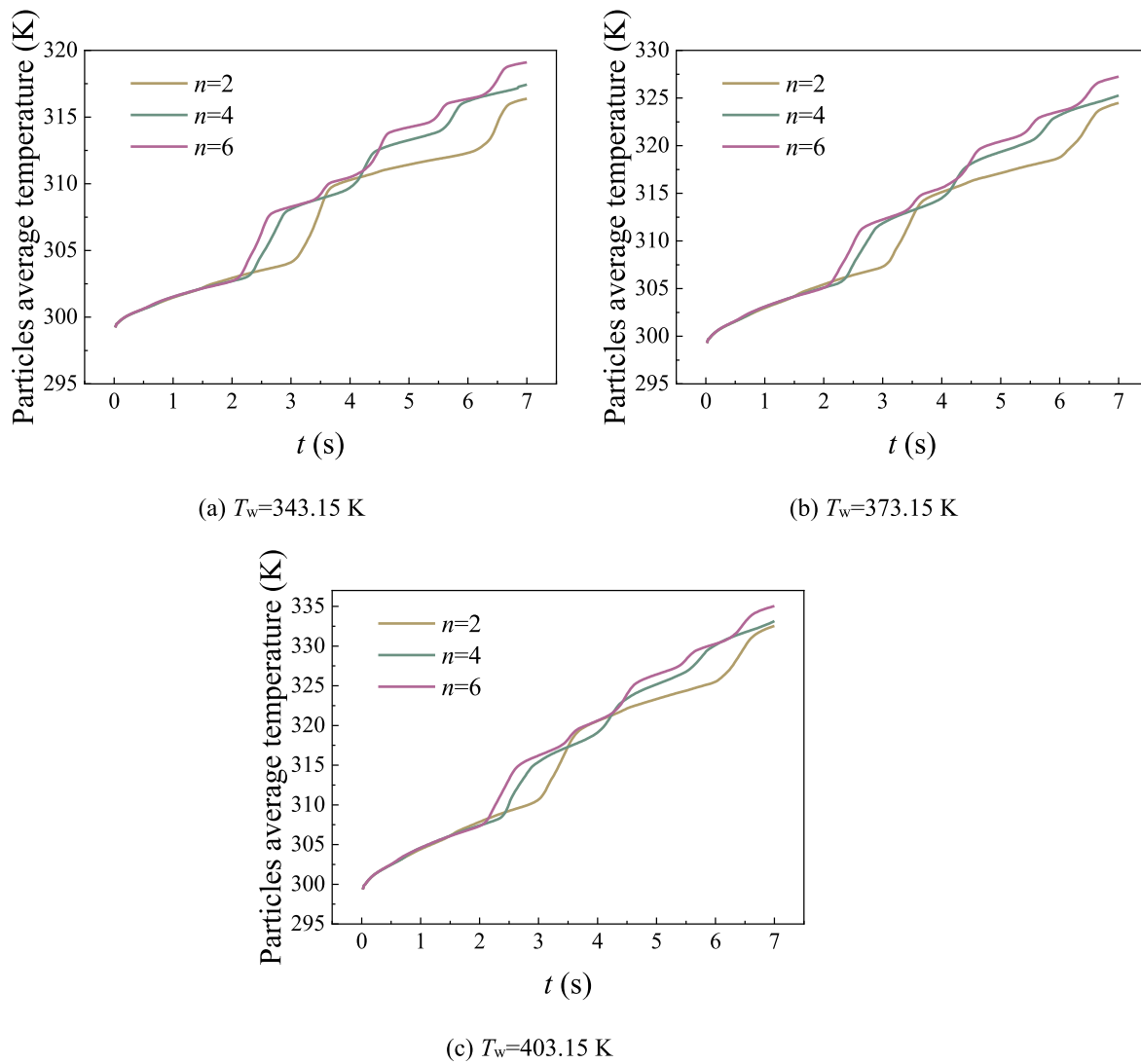


Fig. 12. Average particle temperature variation with time at different baffle numbers.

smallest grid size being 4 mm and the largest 6 mm, all of which were more than three times the particle diameter (0.5 mm), meeting the requirements of the CFD-DEM coupling simulation. For the drum models with different grid densities, air at an inlet velocity of $u_g = 3\text{ m/s}$, an inlet temperature of $T_g = 373.15\text{ K}$, and the wall temperature $T_w = 373.15\text{ K}$ were set. The initial temperature of the flow field inside the drum was set at $T_1 = 298.15\text{ K}$, with a time step of $1 \times 10^{-3}\text{ s}$. The simulation was considered converged when the residuals of all parameters were below 10^{-6} and no longer changed after 0.5 s of calculation.

2.7. Simulation settings

The rotary drum model used in this study has a diameter of 330 mm and a wall thickness of 50 mm. To investigate the influence of the number of baffles on heat transfer, simulations were conducted with configurations containing 2, 4, and 6 baffles. All baffles are evenly distributed along the inner circumference of the drum, with each baffle measuring 20 mm in height and 10 mm in thickness. Approximately 8500 deformable high aspect-ratio biomass particles are loaded into the drum, with the initial arrangement generated through gravitational deposition to ensure a uniform spatial distribution. A schematic diagram of the simulated drum structure and baffle configurations is provided in Fig. 4.

The fluid phase is solved using the finite volume method (FVM), with

the SST $k-\omega$ turbulence model. The drum inlet and outlet are set as velocity inlet and pressure outlet, respectively, while the drum walls are set as constant wall temperature. The pressure-velocity coupling is handled by the Phase Coupled SIMPLE algorithm, and the drag force model used is the Morsi-Alexander model. The particle phase is solved using DEM. To ensure particle stability and the accuracy of the coupled calculations, the DEM time step was set to $5.0 \times 10^{-6}\text{ s}$, and the CFD time step was set to $5.0 \times 10^{-5}\text{ s}$. Data transfer between CFD and DEM is carried out through the coupling interface. The Young's modulus of tobacco leaves is taken from Henry et al. (2000). Restitution and friction coefficients are adopted from typical literature values and summarised in Table 4 (Wu et al., 2020). The drum parameters are set according to relevant standards. Additional simulation parameters, including initial and boundary conditions, and the material parameters, were determined according to values reported in standard materials handbooks, and are presented in Table 5.

To quantitatively evaluate the mixing behaviour, the Lacey Mixing Index was adopted. The simulation domain was divided into sampling cells, and the number of particles in each cell was counted. The index was calculated as follows (Jin et al., 2022):

$$M = \frac{S^2 - S_0^2}{S_r^2 - S_0^2} \quad (52)$$

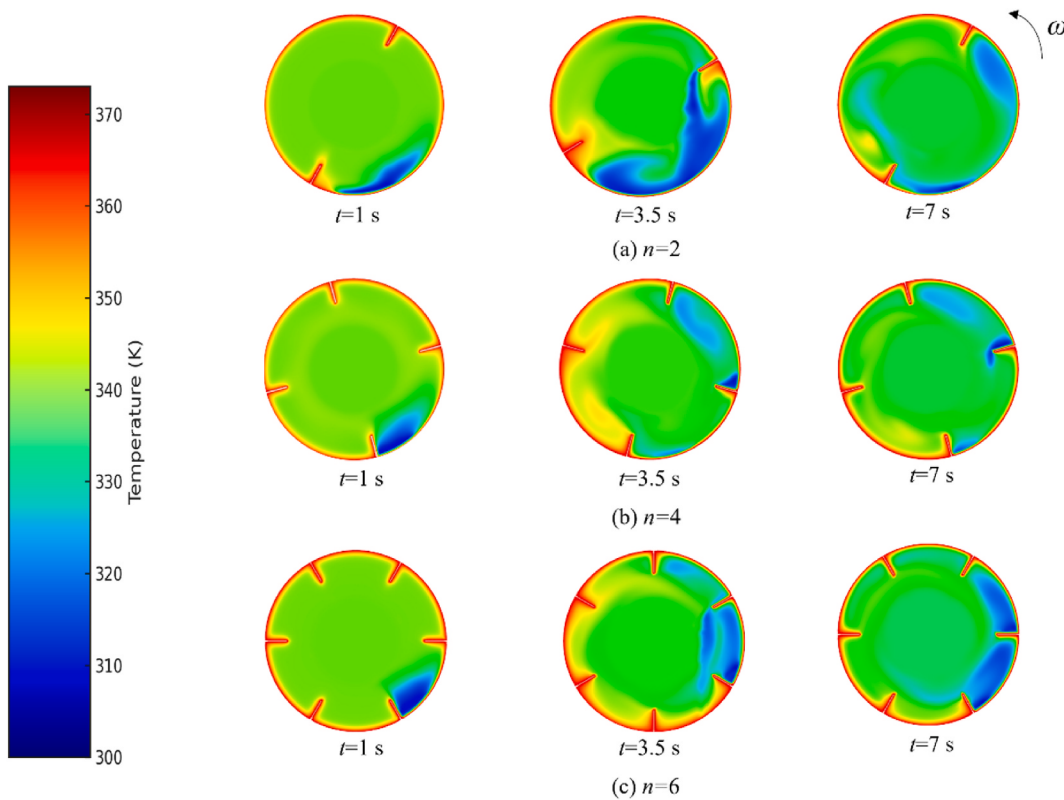


Fig. 13. Simulated temperature contours of particles at different baffle numbers and heating times: (a) $n = 2$; (b) $n = 4$; (c) $n = 6$ ($T_w = 373.15$ K).

where, $S_0^2 = c(1 - c)$, $S_r^2 = c(1 - c)/n_p$, $S^2 = \frac{1}{N-1} \sum_{k=1}^N (c_k - c)^2$ are the variances when the particles are completely separated, completely mixed, and the variance of the current time, respectively. N is the number of cells, n_p is the average number of particles within the cells, c_k is the concentration of a certain type of particle in cell k , and c is the average concentration of that type of particle.

3. Results

3.1. Model validation

The particle temperature curve obtained from the simulation is compared with the experimental values in Fig. 5.

It can be observed from Fig. 5 that the simulated filament temperature curves at different heating temperatures match well with the experimental data. To assess the predictive performance of the thermal conduction model, the mean absolute percentage error was adopted as a quantitative indicator of the fit between simulation and experiment. At heating temperatures of 323.15 K, 333.15 K, and 343.15 K, the respective errors were 4.36 %, 5.18 %, and 6.58 %. These consistently low values, each remaining below 7 %, indicate that the model reliably captures the thermal behaviour of deformable biomass particles with high aspect ratios. The results confirm that the developed model offers both accuracy and robustness across varying thermal conditions.

3.2. Grid independence verification results

The resulting time-dependent airflow pressure at the centre of the drum is shown in Fig. 5. From Fig. 6, it can be seen that for the coarse (65,674), medium (126,928), and fine (197,311) mesh models, the total airflow pressure at the centre point differs only slightly. After calculation, the maximum relative deviation in total pressure between the coarse and fine meshes after stabilisation is less than 1 %. The coarse mesh shows a slight difference compared to the medium and fine

meshes, while the airflow pressure curves for the medium and fine meshes nearly overlap, indicating that the simulation results are independent of the mesh density. Considering both computational accuracy and efficiency, the medium-sized mesh model was chosen for all three drum configurations.

3.3. Effect of drum rotation speed on particle heat transfer

The drum rotation speed directly affects the mixing efficiency of the particles, the frequency of particle-wall collisions, and the frictional forces between the particles (Lange et al., 2024; Zhang et al., 2021). Therefore, in this study of the heat transfer characteristics of deformable high aspect-ratio particles in the drum, four rotation speeds: 6 r min⁻¹, 8 r min⁻¹, 10 r min⁻¹, and 12 r min⁻¹ were selected for comparative analysis, based on parameters from actual industrial processes. Fig. 7 presents the temperature distribution of the deformable high aspect-ratio biomass particle system under different drum rotation speeds and time points. As time progresses, the overall temperature of the particle system gradually increases, with the thermal field extending from the drum wall towards the interior of the particle bed. At 10 and 12 r min⁻¹, the temperature distribution becomes more uniform, and the heating within the particle interior is more evident. This suggests that faster drum rotation enhances particle mixing and contact, thereby facilitating heat conduction between particles. In contrast, at 6 r min⁻¹, heat tends to accumulate near the drum wall, while the temperature rise within the particle interior is slower, leading to lower heat transfer efficiency.

Fig. 8 shows the variation in the average particle temperature with time at different drum rotation speeds. It can be observed that the average particle temperature increases in a stepwise manner at different rotation speeds, with varying rates of temperature increase at different time intervals. After 7 s of rotation, the average temperature of the particles is highest at a rotation speed of $\omega = 12$ r min⁻¹, while the lowest average temperature occurs at $\omega = 6$ r min⁻¹. The calculated final

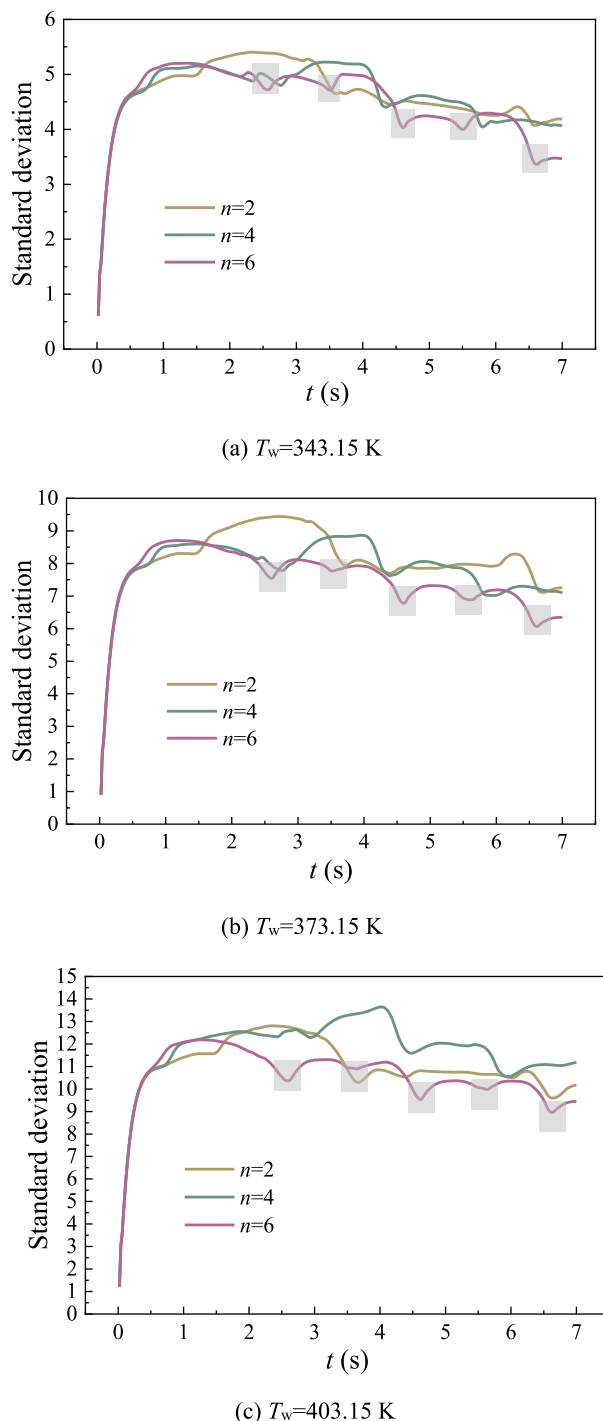


Fig. 14. Temperature standard deviation of particles with time at different baffle numbers.

average temperature of the particles at $\omega = 6 \text{ r min}^{-1}$ is $T_{\omega 6} = 312.50 \text{ K}$, which is 1.86 K lower than the final average temperature at $\omega = 10 \text{ r min}^{-1}$. The final temperatures of the particles at $\omega = 8 \text{ r min}^{-1}$ and $\omega = 12 \text{ r min}^{-1}$ are 314.36 K and 317.07 K, respectively. These results indicate that increasing the drum rotation speed can improve the heat transfer efficiency of the particles. As the rotation speed increases, particle-wall and particle-particle contact increase, enhancing heat conduction and generating more heat.

Fig. 9 shows the variation in particle movement, mixing, and average temperature within the drum at different rotation speeds, where the Mixing index represents the Lacey mixing index of the particles at

different time intervals within the drum. From Fig. 9, it can be seen that the variation in particle temperature is closely related to the mixing index of the particles. When the particles complete their tossing motion in the drum, there is a significant change in the mixing index, which is followed by a change in the particle temperature. Taking $\omega = 10 \text{ r min}^{-1}$ as an example, the particles complete their tossing motion in about 2 s, after which the mixing index rises as the tossing is completed. When the mixing index stabilises, the average particle temperature begins to increase significantly. During the first tossing phase, the mixing index increases by an average of 0.12, and the average temperature rises by 4.8 K, as shown in Fig. 9(c).

From Fig. 9, at a drum rotation speed of $\omega = 10 \text{ r min}^{-1}$, the particles exhibited the most stable and uniform mixing behaviour, as reflected by the consistently high Lacey mixing index and minimal fluctuations over time. On the one hand, when the particles are well mixed, the frequency and opportunity of particle-particle contacts increase, providing more effective pathways for heat exchange and thereby promoting heat transfer. A well-mixed particle system facilitates more uniform heat transfer from high-temperature particles to those at lower temperatures. As shown in Fig. 9, under a rotation speed of $\omega = 10 \text{ r min}^{-1}$, the Lacey mixing index remains relatively high (approximately 0.6) with minimal fluctuation over time, indicating a more homogeneous and stable mixing state. This favourable mixing condition enhances the frequency of particle displacement, thereby increasing the number of thermal contact pathways between particles and reducing localised temperature gradients. Consequently, the rate of heat diffusion within the system is accelerated. Furthermore, improved mixing promotes convective heat exchange both among particles and between particles and the surrounding gas, enhancing the continuity and uniformity of heat transfer throughout the system and thus contributing to improved overall thermal efficiency (Moreno et al., 2016). These results clearly demonstrate that higher drum rotation speeds promote particle mixing, which in turn strengthens heat transfer efficiency.

Fig. 10 shows the process of particle motion in the drum, including “pickup-rotation-tossing-pile-up.” As shown in the figure, when most of the particles remain on the baffles and have not yet begun to be tossed, their temperatures are concentrated around the initial temperature of 298.15 K. Only a small portion of the particles, located near the inner side of the baffles and in contact with the drum wall, have temperatures slightly higher than the initial temperature. When the particles are tossed, both the particles in the tossing phase and those that come into contact with the drum bottom experience an increase in temperature. During the tossing phase, as the particles begin to be lifted by the baffles, their horizontal movement distance increases. During the falling process, the contact area between the particles and the drum wall gradually decreases, and the heat transfer process shifts from conduction with the wall to convection with the hot air (Seidenbecher et al., 2021; Zhang et al., 2021). Therefore, the particle temperature increases during the tossing phase. During the tossing phase, the particles falling onto the drum bottom undergo convective heat transfer during descent and subsequently experience conductive heat transfer upon contacting the heated wall. In contrast, airborne particles rely solely on convective heat exchange, which is comparatively less effective. As a result, the particles at the drum bottom generally exhibit higher temperatures than those in the tossing phase.

Fig. 11(a–c) shows the average temperature of particles at different positions in the drum at various times during the tossing process. The particle motion in the drum is divided into three stages: the preparation stage (A), the tossing stage (B), and the post-tossing stage (C). In stage A, most of the particles are concentrated and piled up on the baffles, with only a small number of particles, due to gravity, sliding into the drum. As shown in Fig. 10(a), the particles piled up on the baffles are divided into two parts: A1, which are the particles piled up on the baffles but not in direct contact with the drum wall, and A2, which are the particles in direct contact with the drum wall. A3 represents the small number of particles that have slid down. During the tossing stage, B1 represents the

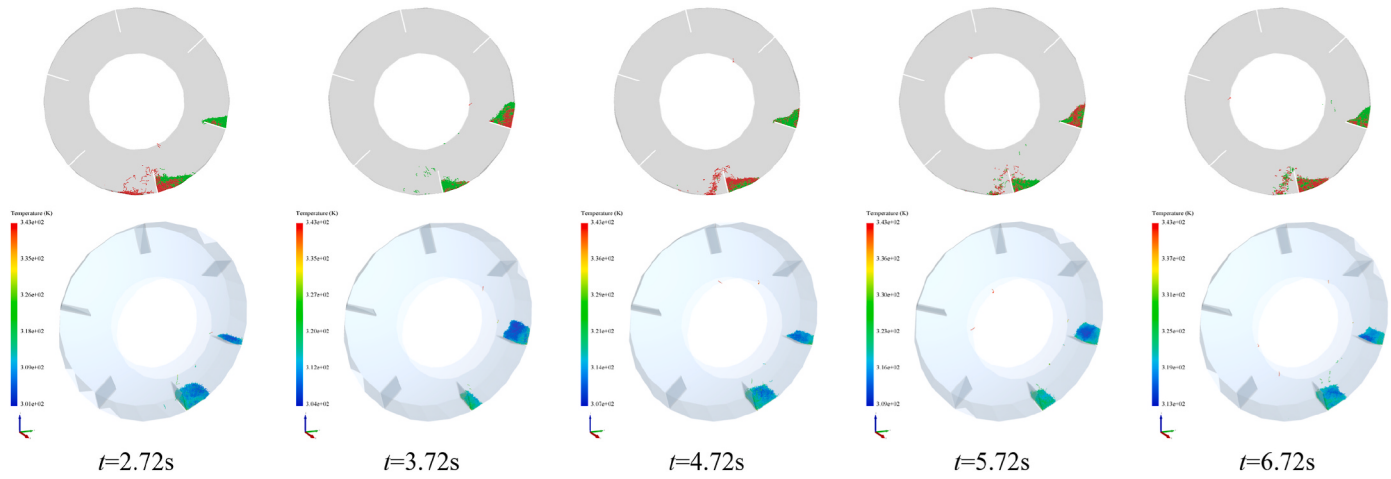


Fig. 15. Images at the end of particle dispersion.

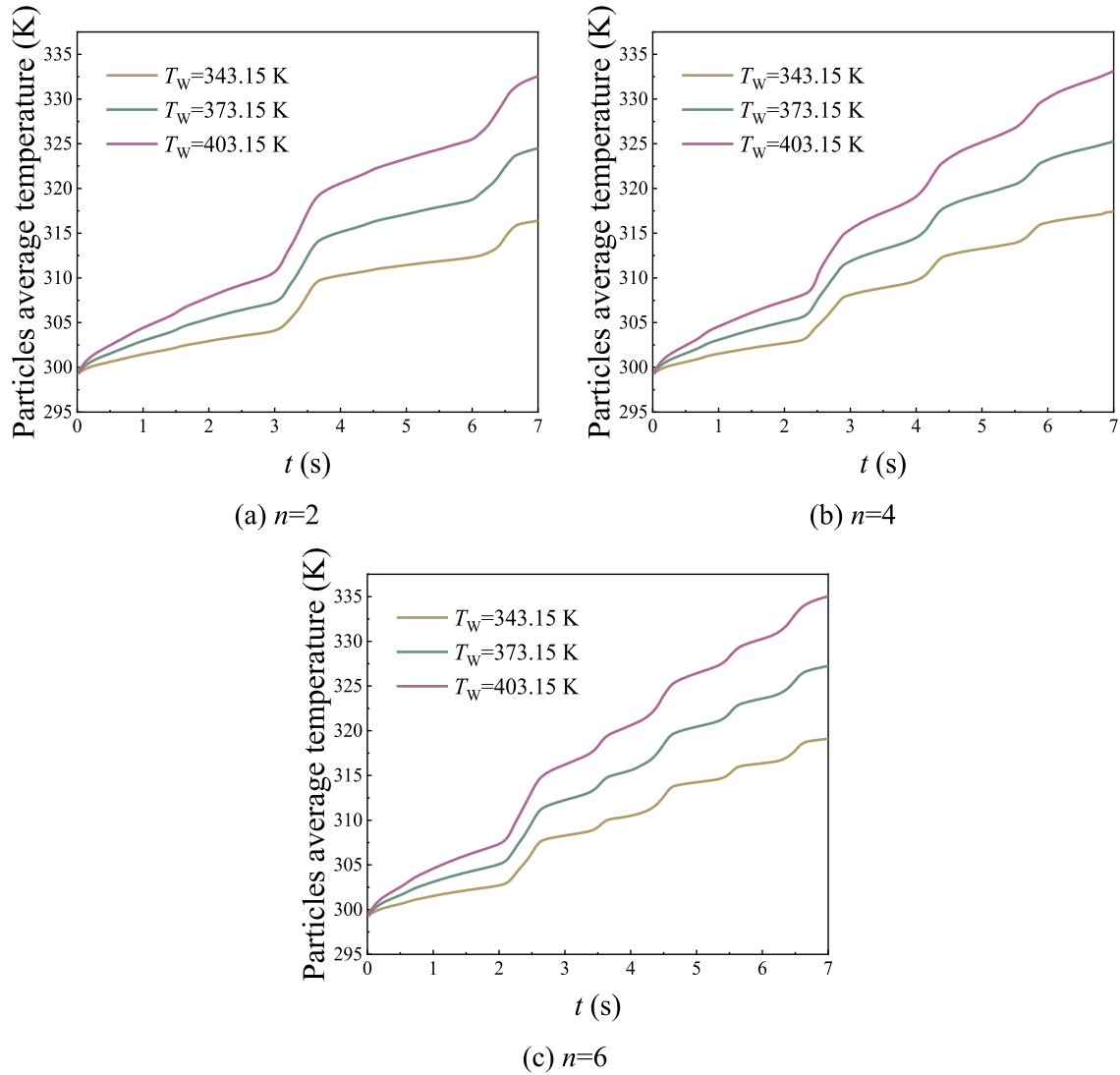


Fig. 16. Average particle temperature versus time at different drum wall temperatures.

particles remaining on the baffles, B2 represents the particles that are being tossed and falling, and B3 represents the particles that have fallen to the bottom of the drum. After the tossing phase is completed, some

particles pile up on the baffles, as shown in C1 in Fig. 11(c), while others pile up at the bottom of the drum, as shown in C2.

Fig. 11(d) shows the data for the first tossing of particles under the

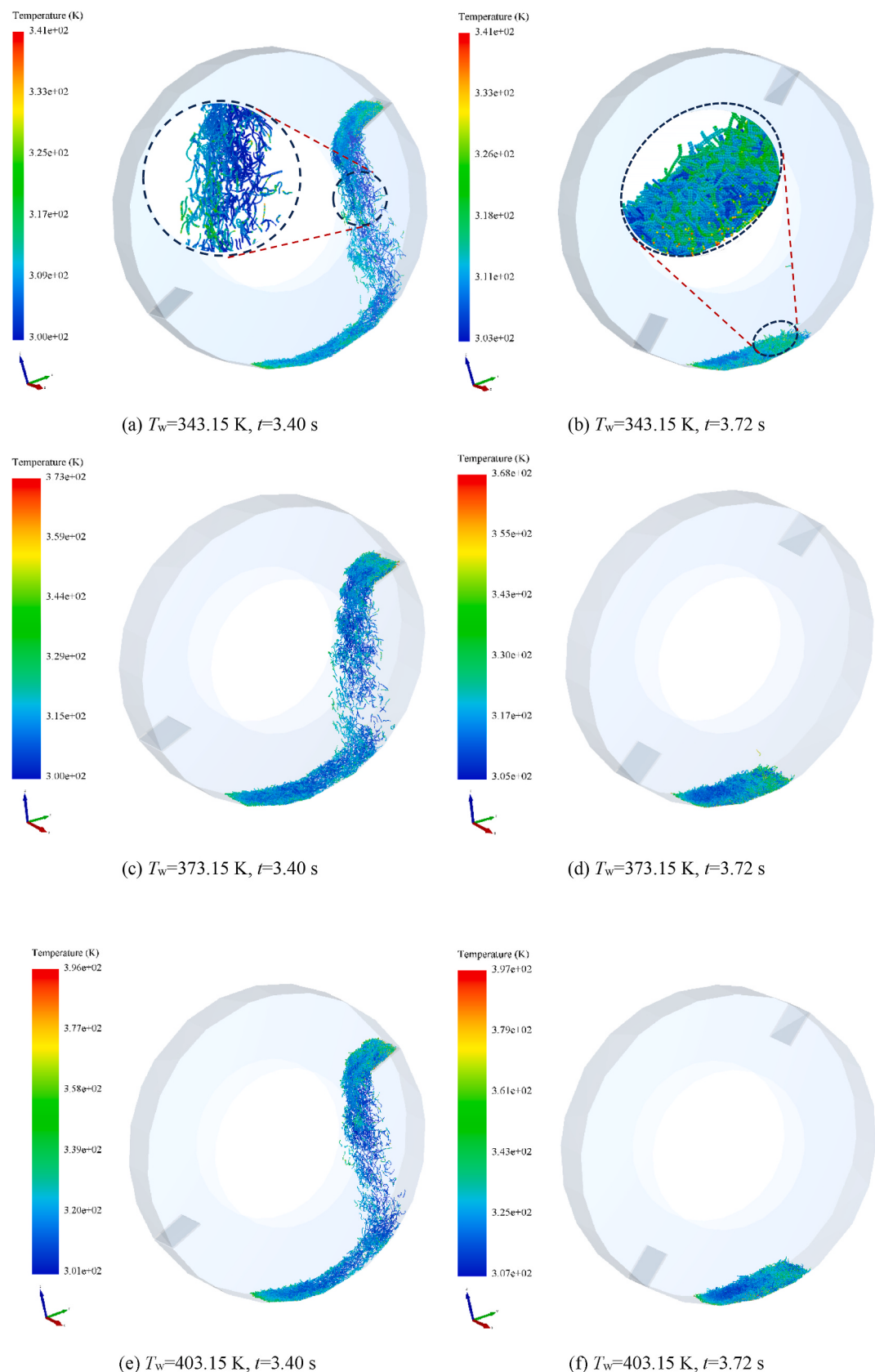


Fig. 17. Flow heating process of particles in the drum at different wall temperatures.

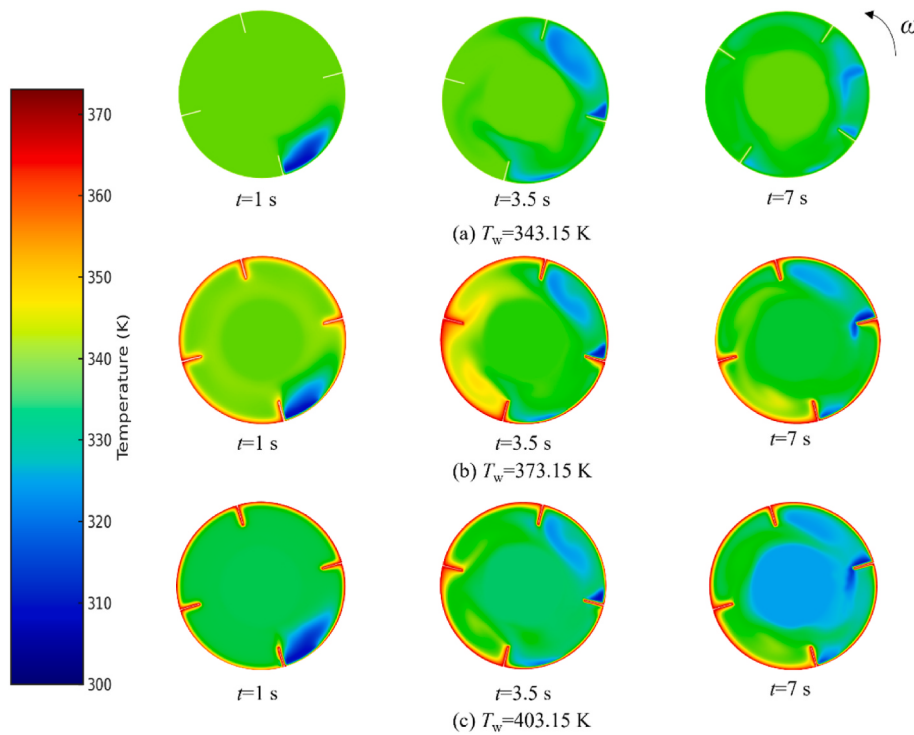


Fig. 18. Simulated temperature contours of biomass particles at different wall temperatures and time point.

condition of $n = 4$, $\omega = 6 \text{ r min}^{-1}$. From the figure, it can be seen that when the particles have not yet started tossing, the average temperature of the A2 particles is 2.85 K lower than that of the A1 particles. This is because when the particles are in direct contact with the drum wall, in addition to the convective heat transfer between the particles and the hot air and the conductive heat transfer between the particles, there is also conductive heat transfer with the drum wall, causing the temperature of this portion of the particles to be higher than that of the particles not in direct contact with the drum wall. The average temperature of the A3 particles is 2.18 K higher than that of the A2 particles, because the particles in A3 are subject to convective heat transfer with the hot air in the drum, and the effect of convective heat transfer on the temperature increase is greater than that of conduction.

When the particles are in the tossing stage, the average temperature of the B1 particles, which remain on the baffles and have not yet been tossed, is 1.41 K and 6.75 K lower than that of the B2 and B3 particles, respectively. This is because the B2 particles experience convective heat transfer with the hot air, while the B3 particles first undergo convective heat transfer with the air and then conductive heat transfer with the drum wall when they land on the bottom. Therefore, the average temperature of the B2 and B3 particles is higher than that of the B1 particles, with the B3 particles having a higher average temperature than the B2 particles. When the tossing is completed, the average temperature of the C1 particles is 5.77 K lower than that of the C2 particles. From Fig. 8(c), it can be seen that the C1 particles are more densely packed than the C2 particles, and the C2 particles are more fully exposed to convective heat transfer with the hot air and conductive heat transfer with the drum wall.

From Fig. 11(d), it can be seen that at different stages of the tossing process, the average temperature of the particles on the baffles is always lower than that of the particles that are falling or have landed on the drum bottom. As the tossing process progresses, the average temperature of the particles gradually increases.

During the preparation stage, the average temperature of the particles is 303.09 K, which is 1.57 K and 6.92 K lower than that in the tossing and post-tossing stages, respectively. As the particles go through the “tossing-pile-up” process in the drum, the particles constantly collide

with the high-temperature drum wall, causing the overall temperature of the particles to continuously rise.

In summary, appropriately increasing the drum rotation speed can enhance the heat transfer efficiency of the particles, but an increase in rotation speed may also inhibit particle mixing. As the tossing process progresses, the average temperature of the particles shows a stepwise increase at different rotation speeds.

3.4. Effect of baffle number on particle heat transfer

This study considers the heat transfer behaviour of deformable high aspect-ratio particle groups in the drum under three different baffle numbers: $n = 2, 4$, and 6 . Fig. 12 shows the variation in average particle temperature with time in the drum at the same wall temperature but with different baffle numbers. From the figure, it can be seen that under the same wall temperature, the more baffles there are, the faster the particle temperature increases. This is because the number of baffles influences the number of times the particles are tossed. The more times the particles are tossed, the more convective heat transfer occurs with the incoming hot air, leading to a faster temperature increase. Therefore, increasing the number of baffles can improve the heat transfer efficiency of particles in the drum (Ardalani et al., 2023; Scherer et al., 2016).

Fig. 13 illustrates the temperature distribution of the particle system inside the drum at different baffle numbers and heating stages, corresponding to the early, middle, and late periods of the heating process. It can be observed that with the increase in both heating time and the number of baffles, the overall temperature of the particle system rises, and the temperature distribution becomes progressively more uniform. Under the condition of $n = 2$, heat is mainly concentrated in the region near the drum wall, while the temperature rise in the inner regions is relatively slow, indicating limited heat transfer. In contrast, with $n = 6$, heat is more effectively conducted into the particle bed, resulting in a more uniform temperature field. This demonstrates that increasing the number of baffles significantly enhances the particle tossing frequency and mixing intensity, thereby improving convective heat transfer with the hot air as well as conductive heat transfer between particles.

Temperature uniformity and heat transfer efficiency are crucial

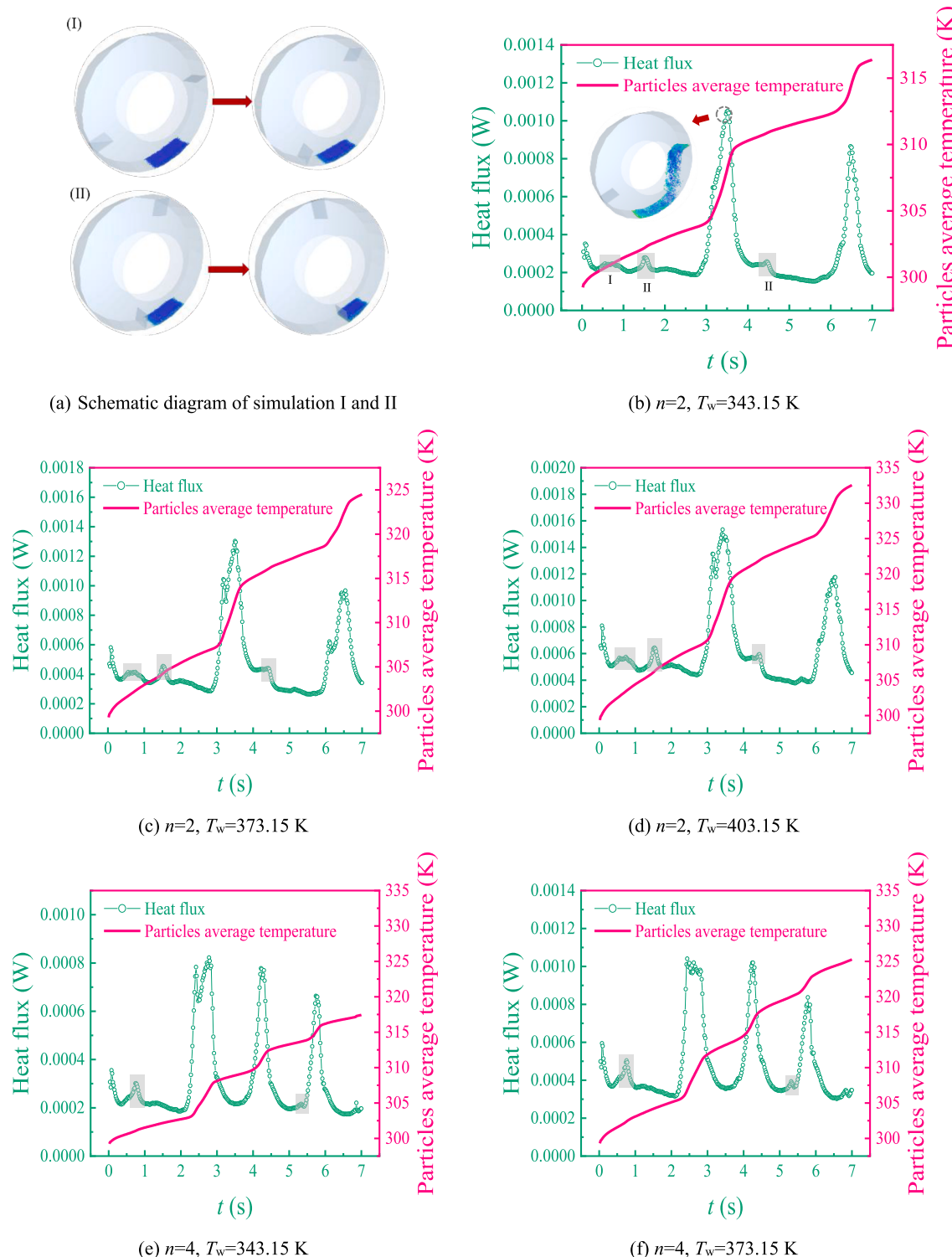


Fig. 19. The variation of average heat flux and temperature of particles over time.

during the drying process of particles in the drum. Uneven particle temperature directly leads to uneven moisture evaporation in different parts of the material, ultimately affecting the drying effectiveness. To study the temperature uniformity, the temperature standard deviation was used for analysis. Fig. 14 shows the variation in temperature standard deviation of particles with time during heating in the drum with different baffle numbers. From the figure, it can be seen that in the initial

heating stage, the temperature standard deviation rises sharply. As the drum rotates and particle mixing occurs, the standard deviation gradually decreases. This is because, in the initial heating stage, the particles near the wall experience a rapid temperature rise due to conduction, while the internal and upper-layer particles increase in temperature more slowly, widening the temperature difference within the particle group. Once the drum reaches the tossing angle and the particles begin

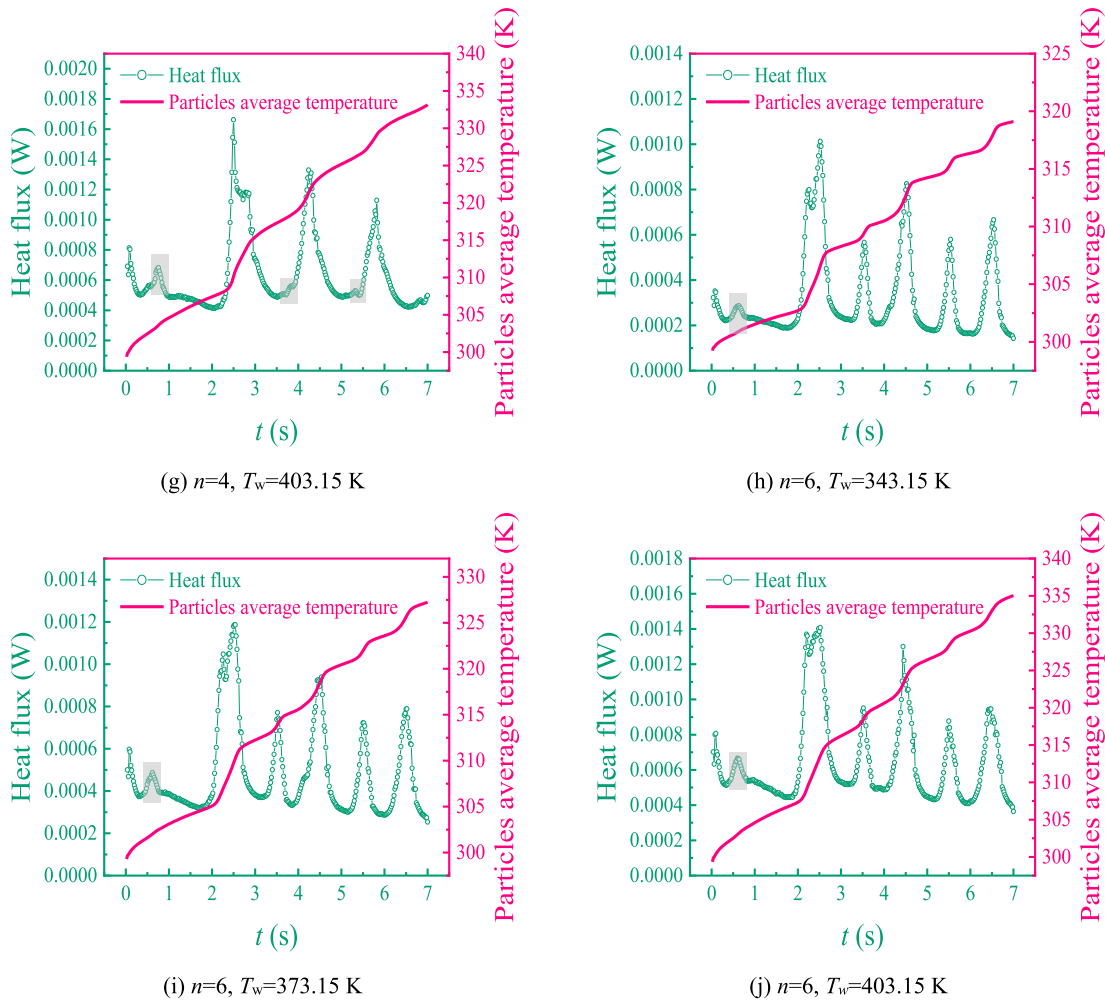


Fig. 19. (continued).

to toss and mix, the contact area with the hot air increases, and the temperatures of different parts of the particles become more uniform, reducing the temperature standard deviation (Xu et al., 2020). Additionally, longitudinal comparison shows that at a wall temperature of $T_w = 373.15 \text{ K}$, the temperature standard deviation is higher than at $T_w = 343.15 \text{ K}$, and at $T_w = 403.15 \text{ K}$, the temperature standard deviation is higher than at $T_w = 373.15 \text{ K}$. This is because higher wall temperatures enhance the heating ability of the particles near the wall, further increasing the temperature difference between the inner and outer layers of the particles.

From Fig. 14, it can be observed that the temperature standard deviation of the particles decreases continuously over time for all baffle configurations. Moreover, the higher the number of baffles, the faster the temperature standard deviation decreases. In the $n = 6$ case, the decrease in the temperature standard deviation is notably faster than in the other configurations. This is because increasing the number of baffles leads to more particle tosses and more contact times with the hot air, which not only promotes uniform mixing but also reduces the temperature difference between the inner particles and the outer high-temperature particles. Therefore, increasing the number of baffles accelerates the process of achieving uniform particle temperature.

In addition, Fig. 14 reveals that the standard deviation of the filamentous particle temperature exhibits a fluctuating downward trend over time. Analysis of the particle motion within the drum shows that each decline in temperature standard deviation roughly corresponds to the moment when particle tossing is completed. Taking the case of $n = 6$ as an example, Fig. 15 presents the mixing state and temperature

distribution of particles at the moment of toss completion in the drum with six baffles. Combined with the standard deviation curve for $n = 6$ in Fig. 14, it can be observed that a distinct reduction in temperature standard deviation occurs after each particle toss. Moreover, the lowest points of the curve align with the airborne phase of the filamentous particles, as indicated by the grey dashed in Fig. 14. This further confirms that the uniformity of particle temperature is closely related to the uniformity of particle mixing. The similarity between the single-phase mixing and the gas-solid coupled mixing behaviour also suggests that the presence of air in the drum has little influence on particle mixing.

3.5. Effect of wall temperature on particle heat transfer

The wall temperature of the drum affects the heat transfer efficiency between the particles and the wall, the uniformity of the internal particle temperature, and the radiation and conduction mechanisms (Adepu, Chen, et al., 2021). Therefore, based on practical industrial parameters, three wall temperatures of 343.15 K, 373.15 K, and 403.15 K were considered to study the heat transfer behaviour of deformable high aspect-ratio particles in the drum. Fig. 16 shows the variation in average particle temperature over time under different drum wall temperatures. From the figure, it can be observed that, with the same number of baffles, the higher the drum wall temperature, the higher the average particle temperature. The final particle temperature is 8.03 K higher at $T_w = 373.15 \text{ K}$ compared to $T_w = 343.15 \text{ K}$, and 7.91 K higher at $T_w = 403.15 \text{ K}$ compared to $T_w = 373.15 \text{ K}$.

From Fig. 16, it can be observed that the overall average temperature

of the particles increases in a stepwise manner, with different rates of temperature rise in each time period. Based on the movement and throwing behaviour of the particles in the drum, it can be seen that when the particles are in the packed lifting state, the rate of temperature rise is slower. When the drum reaches the particle throwing angle, the particles begin to be thrown and fall, and the rate of temperature rise increases significantly. Fig. 17 shows the heating process of particles flowing in the drum under different wall temperatures. When the particles complete one throw in the drum, at $T_w = 343.15$ K, the average temperature rise of the particles is 5.79 K, which is 0.77 K and 3.26 K lower than those at $T_w = 373.15$ K and $T_w = 403.15$ K, respectively. As the drum wall temperature increases, the temperature difference between the particles and the wall increases, enhancing the driving force for heat transfer. This results in more rapid heat conduction from the wall to the surface of the particles and gradually diffuses into the interior, leading to an increase in particle temperature. Therefore, increasing the wall temperature of the drum can significantly raise the particle temperature.

Fig. 18 illustrates the temperature distribution of the particle system at different time points under various drum wall temperatures, corresponding to the early, middle, and late stages of the heating process. It can be observed that as the wall temperature increases, the overall temperature level of the particle system rises significantly, with the thermal field gradually expanding from the region near the drum wall towards the interior of the particle bed. At 343.15 K, heat is mainly concentrated in the outer region of the particle layer, while the temperature rise in the inner region is relatively slow, indicating a limited heat transfer range. In contrast, at 403.15 K, heat spreads more effectively throughout the particle bed, resulting in a more uniform temperature distribution. These results suggest that increasing the wall temperature enhances the conduction rate between the drum wall and the particles, increases the heat flux received by the particle surface per unit time, and promotes the transfer of heat into the particle interior, thereby significantly improving both the heat transfer efficiency and the temperature uniformity of the particle system.

The variation of average heat flux and particle temperature over time is shown in Fig. 19. The data show a strong correlation between the rate of temperature increase and the heat flux. As shown in Fig. 19(b), during the 3–4, the particles are in the tossing phase, during which the temperature rise rate increases significantly, and the average heat flux simultaneously shows a sharp increase. In contrast, during the 4–6, the particles gradually enter the stacking phase, the temperature rise rate tends to stabilise, and the heat flux also levels off accordingly.

From Fig. 19, it can be observed that after the rotary drum starts rotating, the particle heat flux initially decreases from a high value and then experiences several small fluctuations, as shown in shaded areas I and II in Fig. 19. When the particles are at the bottom of the drum, they are lifted by the wall friction. As the height increases, the slope of the wall increases, and when the friction force reaches a critical value, the particles slide down to the bottom, as shown in Fig. 19(a). This heat flux fluctuation only occurs when the number of baffles is 2, because as the number of baffles increases, the sliding process of particles is gradually replaced by the baffle scattering. When particles come into contact with the baffle before reaching the sliding critical value, they are stacked on the baffle as the drum rotates, as shown in shaded area II, reducing the number of heat flux fluctuations. When particles are scattered and come into broad contact with the heated wall, the heat flux increases sharply, forming a distinct peak, as shown in Fig. 19(b). When the number of baffles increases to $n = 6$, there is only one fluctuation before the particles are first scattered, as shown in Fig. 19(h), (i), (j). This is because with more baffles, the particle motion is mainly influenced by the baffle scattering, reducing the contact time and friction with the wall, thereby decreasing the frequency of fluctuations.

From the perspective of heat flux, this sliding process can improve the particle heat transfer efficiency to some extent. This phenomenon shows that while reducing the fluctuations in particle heat flux, the baffles help improve the overall heat transfer efficiency (Jiang et al.,

2024). The increase in the number of baffles shifts the particle movement mode from sliding to scattering, thus reducing the contact time and friction with the wall, facilitating more uniform heat exchange between particles and the wall.

When the drum wall temperature increases, the temperature difference between the particles and the wall increases, enhancing the heat transfer driving force. As a result, heat is transferred more quickly from the wall to the particle surface, raising the particle temperature. This leads to more uniform heating and improved heat transfer efficiency.

4. Discussion

This study conducted a coupled CFD-DEM simulation to investigate the heat transfer behaviour of deformable high aspect-ratio fibre-like biomass particles within a rotary drum dryer. The heat transfer mechanisms were systematically explored from the perspectives of particle modelling, the spatiotemporal distribution of particle temperature, and the interplay between mixing and thermal behaviour. Compared to existing DEM-based studies on particulate systems, this work demonstrates greater physical fidelity and application potential in terms of both modelling accuracy and mechanistic depth.

Firstly, regarding particle modelling, previous studies have commonly employed rigid spherical or ellipsoidal representations to simulate particle dynamics (Ullah et al., 2019; Wang et al., 2024b; Zhu et al., 2021). While computationally efficient, such simplifications fail to adequately capture the actual behaviour of fibrous biomass during deformation and multipoint contact. In contrast, the flexible dual-sphere-chain model developed herein preserves the geometric features of fibre-like particles while incorporating interparticle flexibility, multipoint contact, and local deformation. This significantly enhances the accuracy of characterising thermal contact area and heat flow pathways. The model offers a more realistic depiction of particle-scale interactions, providing a robust framework for simulating heat and mass transfer in complex plant-derived fibrous materials.

Secondly, unlike conventional approaches that analyse bulk-averaged particle temperatures across the domain, this study introduced a dual “phase–position” partitioning strategy to assess average particle temperature at different motion stages (stacking, lifting, and cascading) and within specific spatial zones of the drum (bottom, middle, and top regions). The results revealed that during the cascading phase, the temperature rise rate was significantly higher, especially near the drum wall, indicating that airborne particles experienced enhanced contact with heated surfaces, thereby facilitating faster thermal acquisition. This spatiotemporal resolution of thermal patterns offers greater mechanistic insight than domain-averaged analyses and provides a more precise basis for understanding heat transfer dynamics in drum systems.

Finally, the Lacey mixing index was introduced to quantify the degree of particle mixing and was dynamically compared with the standard deviation of particle temperature to elucidate the influence of mixing on thermal uniformity. The analysis showed that turning points in the temperature standard deviation often corresponded to key events in the tumbling or cascading process, particularly during periods of increased Lacey index. This indicates that improved mixing contributes to reduced thermal gradients and more homogeneous heat distribution.

This study presents several key advancements. A deformable particle model with flexible connections was introduced to more accurately capture the heating and contact behaviour of fibrous biomass within the drum. Next, rather than relying on bulk-averaged temperature analysis, a refined spatial-temporal partitioning strategy was employed to reveal detailed heat transfer characteristics at different locations and particle movement stages. Then, by coupling the Lacey mixing index with the temperature distribution, an intrinsic relationship between particle mixing behaviour and heat transfer efficiency was established. These developments contribute to a deeper understanding of the heat transfer mechanisms in non-spherical particle systems.

5. Conclusion

In this study, experimental and simulation methods were combined to analyse the behaviour of deformable high aspect-ratio biomass particles in a rotary drum, focusing on the effects of drum rotation speed, baffle number, and drum temperature on particle mixing and heat transfer processes. The study demonstrates that the degree of particle mixing is closely linked to heat transfer efficiency; an increase in mixing promotes heat exchange between particles, thereby enhancing heat transfer performance. A heat transfer model for deformable biomass particles was established and validated, with experimental data compared to simulation results to verify the model's effectiveness, showing good consistency between the two. The following conclusions were drawn.

- (1) Increasing the drum rotation speed significantly improved particle mixing, which in turn facilitated heat exchange between the particles. Experimental results showed that at a rotation speed of 10 r min^{-1} , the heat transfer efficiency of the particles was optimal, suggesting that a moderate increase in rotation speed can effectively improve heat transfer performance.
- (2) The increase in the particle mixing index had a significant impact on heat transfer efficiency. A 0.12 rise in the mixing index led to a 4.8 K increase in particle temperature, indicating that enhanced mixing significantly boosts the heat exchange efficiency between particles.
- (3) An increase in the number of baffles contributed to a more uniform particle temperature distribution. The configuration with 6 baffles resulted in a more even temperature distribution, effectively preventing local overheating. Optimising the drum wall temperature further improved heat transfer, with the optimal configuration found to be a drum wall temperature of 403.15 K.

CRediT authorship contribution statement

Conghui Gu: Writing – review & editing, Supervision, Resources, Project administration, Methodology, Conceptualization. **Yufan Zhang:** Writing – review & editing, Writing – original draft, Formal analysis, Data curation. **Yuan Liu:** Investigation, Formal analysis, Data curation. **Huiqian Yin:** Formal analysis, Data curation. **Xingyu Liang:** Formal analysis, Data curation. **Jingyu Zhu:** Formal analysis, Data curation. **Kaiyuan Deng:** Formal analysis, Data curation. **Zhulin Yuan:** Validation, Supervision.

Data availability statement

Data will be made available on request.

Statement on the use of generative AI and AI assisted technologies in the writing process

No generative AI or AI-assisted technologies were used during the preparation of this work.

Declaration of competing interest

The authors declare that they have no known competing financial interests or personal relationships that could have appeared to influence the work reported in this paper.

Acknowledgements

The authors are grateful for the financial support of the National Natural Science Foundation of China (grant No. 51906092).

References

- Adepu, M., Boepple, B., Fox, B., & Emady, H. (2021). Experimental investigation of conduction heat transfer in a rotary drum using infrared thermography. *Chemical Engineering Science*, 230, Article 116145. <https://doi.org/10.1016/j.ces.2020.116145>
- Adepu, M., Chen, S., Jiao, Y., Gel, A., & Emady, H. (2021). Wall to particle bed contact conduction heat transfer in a rotary drum using DEM. *Comput. Particle Mech.*, 8, 589–599. <https://doi.org/10.1007/s40571-020-00356-z>
- Ai, J., Chen, J.-F., Rotter, J. M., & Ooi, J. Y. (2011). Assessment of rolling resistance models in discrete element simulations. *Powder Technology*, 206, 269–282. <https://doi.org/10.1016/j.powtec.2010.09.030>
- Amos, W. A. (1999). Report on biomass drying technology. No. NREL/TP-570-25885, 9548. <https://doi.org/10.2172/9548>
- Ardalani, E., Borghard, W. G., Glasser, B. J., & Cuitiño, A. M. (2023). Scale-up of heat transfer in a rotary drum equipped with baffles. *Powder Technology*, 429, Article 118879. <https://doi.org/10.1016/j.powtec.2023.118879>
- Ardalani, E., Borghard, W. G., Glasser, B. J., & Cuitiño, A. M. (2024). Heat transfer of cohesive particles in a rotary drum: Effect of material properties and processing conditions. *Powder Technology*, 447, Article 120215. <https://doi.org/10.1016/j.powtec.2024.120215>
- Ardalani, E., Yohannes, B., Borghard, W. G., Glasser, B. J., & Cuitiño, A. M. (2022). DEM analysis of the thermal treatment of granular materials in a rotary drum equipped with baffles. *Chemical Engineering Science*, 251, Article 117476. <https://doi.org/10.1016/j.ces.2022.117476>
- Asakuma, Y. (2013). G144 thermal radiation analysis in packed bed by homogenization method. In *The proceedings of the thermal engineering conference 2013* (pp. 229–230). <https://doi.org/10.1299/jsmet.2013.229>
- Bheda, B., Tronstad, J., & Emady, H. (2025). An experimental setup for studying conduction and radiation heat transfer in a rotary drum. *Chemical Engineering Science*, 302, Article 120786. <https://doi.org/10.1016/j.ces.2024.120786>
- Chaudhuri, B., Muzzio, F. J., & Tomassone, M. S. (2006). Modeling of heat transfer in granular flow in rotating vessels. *Chemical Engineering Science*, 61, 6348–6360. <https://doi.org/10.1016/j.ces.2006.05.034>
- Chen, Z., Wassgren, C., & Ambrose, R. P. K. (2022). Development and validation of a DEM model for predicting impact damage of maize kernels. *Biosystems Engineering*, 224, 16–33. <https://doi.org/10.1016/j.biosystemseng.2022.09.012>
- Cho, Y., & Kong, S.-C. (2025). Modeling physicochemical evolution and motion of biomass particle at pyrolysis stage using overset LBM. *Powder Technology*, 452, Article 120570. <https://doi.org/10.1016/j.powtec.2024.120570>
- Chou, S.-H., Hsiao, S.-S., & Liu, S.-Y. (2025). Experimental study of heat transfer and transport properties of granular material in indirectly heated rotary drums. *International Journal of Heat and Mass Transfer*, 238, Article 126485. <https://doi.org/10.1016/j.ijheatmasstransfer.2024.126485>
- Deen, N. G., Van Sint Annaland, M., Van Der Hoef, M. A., & Kuipers, J. A. M. (2007). Review of discrete particle modeling of fluidized beds. *Chemical Engineering Science*, 62, 28–44. <https://doi.org/10.1016/j.ces.2006.08.014>
- Del Giudice, A., Campora, A., Santangelo, E., Pari, L., Bergonzoli, S., Guerriero, E., Petracchini, F., Torre, M., Paolini, V., & Gallucci, F. (2019). Wood chip drying through the using of a mobile rotary dryer. *Energies*, 12, 1590. <https://doi.org/10.3390/en12091590>
- Deng, K., Gu, C., Zhu, J., Du, M., & Pluitenko, D. (2025). Experimental study on flow behavior of wet elongated biomass particles and aggregation-fragmentation evolution of cluster system in a lifting tube. *Particuology*, 98, 249–264. <https://doi.org/10.1016/j.partic.2025.02.004>
- Du, M., Yang, J., Tao, Y., Xu, B., Gu, C., Zhao, H., Liu, Y., Deng, K., & Zhu, J. (2024). Experimental study on the agglomeration behavior of elongated biomass particles in a lifting tube. *ACS Omega*, 9, 4931–4948. <https://doi.org/10.1021/acsomega.3c08719>
- Fei, H., Hong, G., Yu, A., & Li, J. (2025). An investigation on the similarity theory framework for CFD-DEM simulation in a stirred liquid bath containing particles. *Powder Technology*, 452, Article 120538. <https://doi.org/10.1016/j.powtec.2024.120538>
- Fischer, J., Rodrigues, S. J., Kriegeskorte, M., Hilse, N., Illana, E., Scherer, V., & Tsotsas, E. (2023). Particle-particle contact heat transfer models in thermal DEM: A model comparison and experimental validation. *Powder Technology*, 429, Article 118909. <https://doi.org/10.1016/j.powtec.2023.118909>
- Gao, H., Liu, Y., Zheng, B., Sun, P., You, Y., Qi, X., Mao, M., & Zhao, Q. (2020). Particles' flow characteristics in a drum cooler with heat exchanger tubes: Simulation and comparison with traditional solution. *Journal of Cleaner Production*, 255, Article 120264. <https://doi.org/10.1016/j.jclepro.2020.120264>
- Gu, C., Yao, S., Pan, D., Sun, S., Guan, L., Wu, K., & Yuan, Z. (2019). Experimental research on the drying characteristics of flexible fibrous biomass fuels in the baffled-rotary cylinder. *Energy Fuels*, 33(3), 2285–2292. <https://doi.org/10.1021/acs.energyfuels.8b04241>
- Gu, C., Zhang, Y., Liu, Y., & Yuan, Z. (2025). Numerical investigation on mixing characteristics of S-shaped biomass particles in a rotary drum. *Renewable Energy*, 243, Article 122535. <https://doi.org/10.1016/j.renene.2025.122535>
- Han, F., Wang, M., Ma, X., Yin, L., Chen, D., Liu, Z., & Zhang, R. (2023). Numerical simulation of heat transfer properties of large-sized biomass particles during pyrolysis process. *Helijon*, 9, Article e21255. <https://doi.org/10.1016/j.helijon.2023.e21255>
- Havlík, J., & Dlouhý, T. (2020). Indirect dryers for biomass drying—comparison of experimental characteristics for drum and rotary configurations. *Chemical Engineering*, 4, 18. <https://doi.org/10.3390/chemengineering4010018>

- Henry, Z. A., Zhang, H., Su, B., & Onks, D. O. (2000). Elastic properties of the tobacco leaf. *Journal of Agricultural Engineering Research*, 76, 101–110. <https://doi.org/10.1006/jaer.2000.0536>
- Hou, J., Wang, D., Li, F., Zhao, H., Zhang, J., Jin, L., Zhang, C.-A., Xiang, D., Chen, Y.-N., & Wu, X. (2024). Study on heat and mass transfer characteristics in drying process of drum dryer based on the DEM-CFD coupled method. *Thermal Science*, 28, 4655–4667. <https://doi.org/10.2298/TSCI240419177H>
- Huang, A. N., Cheng, T. H., Hsu, W. Y., Huang, C. C., & Kuo, H. P. (2021). DEM study of particle segregation in a rotating drum with internal diameter variations. *Powder Technology*, 378, 430–440. <https://doi.org/10.1016/j.powtec.2020.10.019>
- Ilłana, E., Qyteti, K., Scharnowski, M., Brömmel, M., Wirtz, S., & Scherer, V. (2024). Shape-changing particles for locally resolved particle geometry in DEM simulations. *Particuology*, 89, 185–190. <https://doi.org/10.1016/j.partic.2023.11.003>
- Jian, Q., Gu, H., Wang, K., Wang, S., Zhan, M., Wang, J., Ji, L., Chi, Z., & Zhang, G. (2024). Numerical study of particle behaviours and heat transfer in a complex rotary kiln. *Particuology*, 92, 81–94. <https://doi.org/10.1016/j.partic.2024.04.004>
- Jiang, H., Yang, S., & Hu, J. (2024). Discrete element method study of the mixing and heat transfer behaviour of a binary-size granular system in a rotating drum. *Canadian Journal of Chemical Engineering*, 102, 3448–3461. <https://doi.org/10.1002/cjce.25262>
- Jin, X., Wang, S., & Shen, Y. (2022). Effects of operating conditions and particle properties on mixing performance in an industrial-scale U-shape ribbon mixer. *Powder Technology*, 411, Article 117933. <https://doi.org/10.1016/j.powtec.2022.117933>
- Kildashki, K., Dong, K., & Yu, A. (2023). Contact force models for non-spherical particles with different surface properties: A review. *Powder Technology*, 418, Article 118323. <https://doi.org/10.1016/j.powtec.2023.118323>
- Kumar, A., Kandasamy, P., Chakraborty, I., & Hangshing, L. (2022). Analysis of energy consumption, heat and mass transfer, drying kinetics and effective moisture diffusivity during foam-mat drying of mango in a convective hot-air dryer. *Biosystems Engineering*, 219, 85–102. <https://doi.org/10.1016/j.biosystemseng.2022.04.026>
- Kuznetsov, G. V., Syrodyo, S. V., Nigay, N. A., Maksimov, V. I., & Gutareva, N. Y. (2021). Features of the processes of heat and mass transfer when drying a large thickness layer of wood biomass. *Renewable Energy*, 169, 498–511. <https://doi.org/10.1016/j.renene.2020.12.137>
- Lange, A., Meitzner, C., Specht, E., & Krugel-Emden, H. (2024). Exploring transverse particle motion in rotary drums: DEM analysis of the influence of cross-shaped internals on material transport. *Powder Technology*, 443, Article 119907. <https://doi.org/10.1016/j.powtec.2024.119907>
- Li, H., He, Y., Tang, T., & Zhai, M. (2023). Prediction of the non-uniform drying of wet grain in a fluidised-bed based on a modified CFD-DEM drying model. *Biosystems Engineering*, 236, 103–119. <https://doi.org/10.1016/j.biosystemseng.2023.10.009>
- Liu, B., Wang, Q., Zhou, Z., & Zou, R. (2022). Influence of baffles on mixing and heat transfer characteristics in an internally heated rotating drum. *Powder Technology*, 398, Article 117129. <https://doi.org/10.1016/j.powtec.2022.117129>
- Ma, H., Zhou, L., Liu, Z., Chen, M., Xia, X., & Zhao, Y. (2022). A review of recent development for the CFD-DEM investigations of non-spherical particles. *Powder Technology*, 412, Article 117972. <https://doi.org/10.1016/j.powtec.2022.117972>
- Menter, F. R. (1994). Two-equation eddy-viscosity turbulence models for engineering applications. *AIAA Journal*, 32, 1598–1605. <https://doi.org/10.2514/3.12149>
- Mindlin, R. D., & Deresiewicz, H. (1953). *Elastic spheres in contact under varying oblique forces*.
- Moreno, R. M., Antolín, G., & Reyes, A. E. (2016). Heat transfer during forest biomass particles drying in an agitated fluidised bed. *Biosystems Engineering*, 151, 65–71. <https://doi.org/10.1016/j.biosystemseng.2016.08.002>
- Morimoto, T., O'Sullivan, C., & Taborda, D. M. G. (2023). Capturing particle-fluid heat transfer in thermo-hydro-mechanical analyses using DEM coupled with a pore network model. *Powder Technology*, 429, Article 118944. <https://doi.org/10.1016/j.powtec.2023.118944>
- Morsi, S. A., & Alexander, A. J. (1972). An investigation of particle trajectories in two-phase flow systems. *Journal of Fluid Mechanics*, 55, 193. <https://doi.org/10.1017/S0022112072001806>
- Murungan, P., Dhanushkodi, S., Sudhakar, K., & H. Wilson, V. (2021). Industrial and small-scale biomass dryers: An overview. *Energy Engineering*, 118, 435–446. <https://doi.org/10.32604/EE.2021.013491>
- Nassauer, B., & Kuna, M. (2013). Contact forces of polyhedral particles in discrete element method. *Granular Matter*, 15, 349–355. <https://doi.org/10.1007/s10035-013-0417-9>
- Pan, H., Chen, X.-Z., Liang, X.-F., Zhu, L.-T., & Luo, Z.-H. (2016). CFD simulations of gas-liquid-solid flow in fluidized bed reactors — A review. *Powder Technology*, 299, 235–258. <https://doi.org/10.1016/j.powtec.2016.05.024>
- Park, S., Chang, S., Oh, S. H., Kim, S. I., & Kim, W. (2024). Dependence of drying rate on interfacial thermal contact conductance in drum drying of thin materials. *International Journal of Heat and Mass Transfer*, 221, Article 125033. <https://doi.org/10.1016/j.ijheatmasstransfer.2023.125033>
- Peukert, W., & Bück, A. (2024). “Green” particle technology: Its history, successes, and open issues. *Powder Technology*, 448, Article 120255. <https://doi.org/10.1016/j.powtec.2024.120255>
- Potyondy, D. O., & Cundall, P. A. (2004). A bonded-particle model for rock. *International Journal of Rock Mechanics and Mining Sciences*, 41, 1329–1364. <https://doi.org/10.1016/j.ijrmms.2004.09.011>
- Rashid, M. T., Liu, K., Jatoi, M. A., Safdar, B., Lv, D., & Li, Q. (2022). Energy efficient drying technologies for sweet potatoes: Operating and drying mechanism, quality-related attributes. *Frontiers in Nutrition*, 9, Article 1040314. <https://doi.org/10.3389/fnut.2022.1040314>
- Romero-Valle, M. A., Goniva, C., & Nirschl, H. (2021). Modeling of non-spherical particle flows: Movement and orientation behavior. *Powder Technology*, 382, 351–363. <https://doi.org/10.1016/j.powtec.2020.11.083>
- Rybak, K., Parniakov, O., Samborska, K., Wiktor, A., Witrowa-Rajchert, D., & Nowacka, M. (2021). Energy and quality aspects of freeze-drying preceded by traditional and novel pre-treatment methods as exemplified by red bell pepper. *Sustainability*, 13, 2035. <https://doi.org/10.3390/su13042035>
- Saruwatari, M., & Nakamura, H. (2022). Coarse-grained discrete element method of particle behavior and heat transfer in a rotary kiln. *Chemical Engineering Journal*, 428, Article 130969. <https://doi.org/10.1016/j.cej.2021.130969>
- Scherer, V., Monnigmann, M., Berner, M. O., & Sudbrock, F. (2016). Coupled DEM-CFD simulation of drying wood chips in a rotary drum – Baffle design and model reduction. *Fuel*, 184, 896–904. <https://doi.org/10.1016/j.fuel.2016.05.054>
- Schirck, J., & Morris, A. (2024a). Heat transfer and flow analysis of a novel particle heater using CFD-DEM. *Powder Technology*, 442, Article 119858. <https://doi.org/10.1016/j.powtec.2024.119858>
- Schirck, J., & Morris, A. (2024b). Heat transfer and flow analysis of a novel particle heater using CFD-DEM. *Powder Technology*, 442, Article 119858. <https://doi.org/10.1016/j.powtec.2024.119858>
- Seidenbecher, J., Herz, F., Meitzner, C., Specht, E., Wirtz, S., Scherer, V., & Liu, X. (2021). Temperature analysis in flighted rotary drums and the influence of operating parameters. *Chemical Engineering Science*, 229, Article 115972. <https://doi.org/10.1016/j.ces.2020.115972>
- Tsotsas, E. (2019). Particle-particle heat transfer in thermal DEM: Three competing models and a new equation. *International Journal of Heat and Mass Transfer*, 132, 939–943. <https://doi.org/10.1016/j.ijheatmasstransfer.2018.12.090>
- Ullah, A., Hong, K., Gao, Y., Gungor, A., & Zaman, M. (2019). An overview of Eulerian CFD modeling and simulation of non-spherical biomass particles. *Renewable Energy*, 141, 1045–1066. <https://doi.org/10.1016/j.renene.2019.04.074>
- Wang, J., Ma, L., Fang, Q., Zhang, C., Chen, G., & Yin, C. (2024a). Convective heat transfer coefficients models for biomass cylindrical particles from low to high aspect ratio. *Applied Thermal Engineering*, 253, Article 123815. <https://doi.org/10.1016/j.aplthermaleng.2024.123815>
- Wang, J., Ma, L., Fang, Q., Zhang, C., Chen, G., & Yin, C. (2024b). Accurate machine-learning-based prediction of aerodynamic and heat transfer coefficients for cylindrical biomass particles. *Chemical Engineering Journal*, 498, Article 155192. <https://doi.org/10.1016/j.cej.2024.155192>
- Wang, J., Ma, L., Fang, Q., Zhang, C., Chen, G., & Yin, C. (2024c). Convective heat transfer coefficients models for biomass cylindrical particles from low to high aspect ratio. *Applied Thermal Engineering*, 253, Article 123815. <https://doi.org/10.1016/j.aplthermaleng.2024.123815>
- Wang, C., Wang, S., Jin, X., Zhang, T., & Ma, Z. (2021). Analytical solution for the heat and mass transfer of spherical grains during drying. *Biosystems Engineering*, 212, 399–412. <https://doi.org/10.1016/j.biosystemseng.2021.11.006>
- Washino, K., Chan, E. L., Tsujimoto, T., Tsuji, T., & Tanaka, T. (2023). Development of resolved CFD-DEM coupling model for three-phase flows with non-spherical particles. *Chemical Engineering Science*, 267, Article 118335. <https://doi.org/10.1016/j.ces.2022.118335>
- Wei, G., Zhang, H., An, X., & E, D. (2020). Numerical investigation on the mutual interaction between heat transfer and non-spherical particle dynamics in the blast furnace raceway. *International Journal of Heat and Mass Transfer*, 153, Article 119577. <https://doi.org/10.1016/j.ijheatmasstransfer.2020.119577>
- Wu, K., Zhang, E., Yuan, Z., Li, B., Zhu, W., Xu, J., Wang, L., & Luo, D. (2020). Analysis of flexible ribbon particle residence time distribution in a fluidised bed riser using three-dimensional CFD-DEM simulation. *Powder Technology*, 369, 184–201. <https://doi.org/10.1016/j.powtec.2020.05.025>
- Xie, Q., Chen, Z., Hou, Q., Yu, A. B., & Yang, R. (2017). DEM investigation of heat transfer in a drum mixer with lifters. *Powder Technology*, 314, 175–181. <https://doi.org/10.1016/j.powtec.2016.09.022>
- Xie, Q., Chen, Z., Mao, Y., Chen, G., & Shen, W. (2018). Case studies of heat conduction in rotary drums with L-shaped lifters via DEM. *Case Studies in Thermal Engineering*, 11, 145–152. <https://doi.org/10.1016/j.csste.2018.02.001>
- Xu, D., Yang, F., Jin, H., Curtis, J. S., & Guo, Y. (2020). An investigation of heat transfer of flexible fibers in a rotating drum dryer using the discrete element method. *Powder Technology*, 364, 494–506. <https://doi.org/10.1016/j.powtec.2020.02.024>
- Yi, J., Li, X., He, J., & Duan, X. (2020). Drying efficiency and product quality of biomass drying: A review. *Drying Technology*, 38, 2039–2054. <https://doi.org/10.1080/07373937.2019.1628772>
- Zare, M., & Hashemabadi, S. H. (2019). CFD simulation and experimental validation of tortuosity effects on pellet-fluid heat transfer of regularly stacked multi-lobe particles. *Chemical Engineering Journal*, 361, 1543–1556. <https://doi.org/10.1016/j.cej.2018.10.188>
- Zhang, L., Jiang, Z., Mellmann, J., Weigler, F., Herz, F., Bück, A., & Tsotsas, E. (2021). Influence of the number of flights on the dilute phase ratio in flighted rotating drums by PTV measurements and DEM simulations. *Particuology*, 56, 171–182. <https://doi.org/10.1016/j.partic.2020.09.010>
- Zhao, H., Du, M., Gu, C., Zhu, J., Deng, K., & Liu, Y. (2024). Study on motion characteristics of filamentous biomass particles in a cyclone separator. *Chemical*

- Engineering Research and Design*, 201, 242–256. <https://doi.org/10.1016/j.cherd.2023.11.044>
- Zhou, X., Fu, J., & Chen, S. (2023). CFD-DEM investigation of flow and heat transfer characteristics in a directly irradiated fluidized bed. *Chemical Engineering Journal*, 476, Article 146631. <https://doi.org/10.1016/j.cej.2023.146631>
- Zhu, J., Gu, C., Du, M., Deng, K., & Pliutenko, D. (2025). Experimental study on the motion characteristics of non-spherical biomass particulate systems in a fluidization tube. *Chemical Engineering Science*, 303, Article 120960. <https://doi.org/10.1016/j.ces.2024.120960>
- Zhu, C.-Y., Yang, W.-X., Xu, H.-B., Ding, B., Gong, L., & Li, Z.-Y. (2021). A general effective thermal conductivity model for composites reinforced by non-contact spherical particles. *International Journal of Thermal Sciences*, 168, Article 107088. <https://doi.org/10.1016/j.ijthermalsci.2021.107088>